Harmonic pumping tomography applied to image the hydraulic properties and interpret the connectivity of a karstic and fractured aquifer (Lez aquifer, France)

P. Fischer, Abderrahim Jardani, H. Jourde, M. Cardiff, X. Wang, S. Chedeville, N. Lecoq

Research Paper/

Harmonic Pumping Tomography Applied to Image the Hydraulic Properties and Interpret the Connectivity of a Karstic and Fractured Aquifer (Lez Aquifer, France)

P. Fischer[1], A. Jardani[1], H. Jourde[2], M. Cardiff[3], X. Wang[2], S. Chedeville[2], N. Lecoq[1]

(1) Normandie Univ, UNIROUEN, UNICAEN, CNRS, M2C, 76000 Rouen, France

(2) Laboratoire Hydrosciences, Université de Montpellier, CNRS, 34000 Montpellier, France

(3) Department of Geoscience, University of Wisconsin-Madison, Madison, WI, USA

Corresponding author: P. Fischer

E-mail : pierre.fischer1@univ-rouen.fr

Conflict of interest: None

Key words: Hydraulic tomography, Karst, Oscillatory signal, Connectivity, Modeling, Conduit network

Intended for publication in Advances in Water Resources

Abstract

In this work, we present a novel method to interpret, at a field scale, the preferential flows generated by harmonic pumping tests, in which the pumped flowrate varies according to a sinusoidal function with a given period. The experimental protocol relies on the application of harmonic pumping tests in a karstic field located near to Montpellier (Southern France) at 4 different boreholes, each time with a shorter and a longer period, and the analysis of the hydraulic responses recorded at the 13 observation wells. A qualitative analysis of the oscillatory component in the hydraulic responses, in term of amplitude decay and phase lag, permitted to propose a preliminary model of degree of connectivity between the boreholes, through the network of conduits. Then, a quantitative interpretation of the harmonic responses was applied to image the spatial heterogeneity of the hydraulic properties (hydraulic conductivity and storage coefficient) by using a deterministic inverse algorithm called CADI. This algorithm is based on an equivalent porous medium concept and parameterized by a Cellular Automata approach in order to provide a realistic reconstruction of the karstic network. This algorithm is linked to the groundwater flow equation, reformulated in frequency domain, to simulate the amplitudes and phase shifts responses to the harmonic pumping tests. The inverse process was successfully applied on the dataset collected with both periods, in a separate and joint way. The results obtained allowed for a discussion on the efficiency of the harmonic pumping tomography for the characterization of the karstic structures.

1. Introduction

The protection and the management of the water resources involve the identification of the preferential flow paths in the ground. Therefore, one needs to characterize the spatial distribution of the hydraulic properties in the field subsurface. A common way to assess the hydraulic properties of a field, such as conductivity and specific storage, is the analysis of the drawdown responses to a pumping test from which local or average properties can be inferred from analytical equations that relate the hydraulic response to the hydraulic properties (Butler 2005).

However, in the case of karstic aquifers, the assessment of the hydraulic properties is challenging (White 2002; Hartmann et al. 2014) as the hydraulic properties in this type of aquifer can vary by several orders of magnitude within a short distance (Wang et al. 2016). This makes the characterization of the karstic fields very complex. To face this difficulty, it is then necessary to interpret the responses of the field by taking into account the positioning of the conduits network, which determines the preferential flow paths (Kovacs 2003; Ghasemizadeh et al. 2012; Saller et al. 2013).

The hydraulic tomography concept has been widely applied to map the spatial variability of hydraulic properties, in both type of aquifers (porous and fractured), by performing a joint interpretation of hydraulic data recorded simultaneously at several wells, as responses to extraction/injection of water (Yeh and Liu 2000; Bolhing et al. 2002; Zhu and Yeh 2005; Yeh and Lee 2007; Cardiff et al. 2009a; Castagna et al. 2011; Berg and Illman 2013; Cardiff et al. 2013a; Zha et al. 2015; Zha et al. 2016; Zha et al. 2017). This approach relies on a numerical technique (such as finite difference, finite element and finite volume) to solve the groundwater flow equation, and the inverse process to reconstruct the heterogeneity of the hydraulic conductivities and the storage properties by fitting the piezometric responses. The

inversion process usually provides a non-unique solution which can produce an ambiguous interpretation of the hydraulic data. To overcome this issue, a prior information on the distribution of the properties can be used to constrain and guide the inversion to a more realistic solution (Carrera and Neuman 1986). In the case of aquifers with a low heterogeneity, the geostatistical constraints remain the most simple and efficient way to find accurate solutions (Hoeksema and Kitanidis 1984; Kitanidis 1995; Fischer et al. 2017a). In the context of fractured and karstic aquifers, the definition of the a priori model, or even the strategy for the numerical groundwater flow simulation (which can be performed by using various techniques such as equivalent porous media or discrete fractures networks), remain the subject of open debates among hydrogeologists. In fact, for a successful interpretation of hydraulic responses of karstic aquifers, the 'classical' geostatistical inversion method would require a dense network of measurement and a significant resolution of model parameterization because of the high contrasts existing in the distribution of the spatial properties. Recently, several inversion methods have been developed for characterizing karst networks. One way is to directly incorporate a discrete geometry within a background model using a discrete-continuum forward model (Teutsch 1993; Liedl et al. 2003; de Rooij et al. 2013). In this case, the parameterization of the inverse problems usually relies on a stochastic generation of discrete fracture networks that are conditioned to statistical (Li et al. 2014; Le Coz et al. 2017), mechanical (Jaquet et al. 2004; Bonneau et al. 2013), or structural data (Pardo-Iguzquiza et al. 2012; Collon et al. 2017). Another way is based on a deterministic optimization of the geometry of discrete networks (Borghi et al. 2016; Fischer et al. 2018a).

Previous studies have shown that equivalent porous media models are able to reproduce the hydraulic flows in karstic aquifers at a kilometric scale (Larocque et al. 1999; Abusaada and Sauter 2013) or a decametric scale (Wang et al. 2016). However, if the scale of investigation is too small, this type of model can become unreliable for the characterization of the

properties of fractured rocks, extremely contrasted and structured at a small scale (Illman 2014). Although the classical geostatistical inverse approaches were originally proposed for inversion of hydraulic fields, they can be made adaptive to discrete geometries with special treatments to the prior model (e.g. the total variation prior model, Lee and Kitanidis 2013), or using an iterative procedure (e.g. the sequential successive linear estimator, Ni and Yeh 2008 ; Hao et al. 2008 ; Illman et al. 2009 ; Sharmeen et al. 2012). Other methods for inversion of complex discrete structures involve introducing constraints of a priori knowledge to the inverse model using a guided image (Hale 2009; Soueid Ahmed et al. 2015), a training image (Lochbühler et al. 2015), a probability perturbation (Caers and Hoffman 2006), a transition probability distribution (Wang et al. 2017), a multi-scale resolution (Ackerer and Delay 2010), a level-set method (Lu and Robinson 2006; Cardiff and Kitanidis 2009b), or based on cellular automata (Fischer et al. 2017b).

Apart from these challenges in modeling techniques, a further difficulty in karst aquifer characterization raises from characteristics of hydraulic tests. Due to the integration nature of pressure diffusion, the steady state responses of long-term constant-rate pumping tests in a karst aquifer represent the combined effect of the multiple media (conduits, fissures, matrix) rather than specific components. Although the interpretation of transient responses may provide additional information about the relative importance of each aquifer components, the inclusion of such data in a modeling in the time domain is also computationally demanding. Recently, harmonic pumping tests have been introduced as an alternative for the identification of the networks of preferential groundwater flows. Harmonic characterization designates an investigation in which an oscillatory/sinusoidal signal is used to disturb the water level of an aquifer. Different ways to produce such signals have already been proposed: a pumping-reinjecting system (Rasmussen et al. 2003; Renner and Messar 2006), a moving mass at the water table interface (Guiltinan and Becker 2015), or a controlled pumping system (Lavenue

and de Marsily 2001). Then, the response signals among the aquifer contain an oscillatory part (characterized by an amplitude and a phase offset values) that can be easily isolated from the ambient noise (Bakhos et al. 2014; Cardiff and Barrash 2015). Harmonic characterization has already been successfully applied to a large range of complex cases such as contaminated aquifer (Rasmussen et al. 2003), leakage detection (Sun et al. 2015), or fractured aquifers (Renner and Messar 2006; Maineult et al. 2008; Guiltinan and Becker 2015). The theoretical aspects of the application of harmonic pumping to karstic aquifers have also been developed in Fischer et al. (2018b). The imagery potential of harmonic investigations has been studied for mapping the distribution of hydraulic properties in heterogeneous aquifers with models solved in the time domain (Lavenue and de Marsily 2001; Soueid Ahmed et al. 2016) or in the frequency domain (Cardiff et al. 2013b; Zhou et al. 2016)

In this article we will present a field characterization of karst network based on a harmonic pumping tomography. Hydraulic data were obtained from the Terrieu experimental site located in Montpellier, in Southern France. At the same site, results of hydraulic tomography, in which hydraulic responses were generated with constant-rate pumping tests, have already been presented and discussed in our previous works (Wang et al. (2016), Wang et al. (2017) and Fischer et al. (2017c)). In this new work, we rely our analysis on a set of responses to harmonic pumping tests with different oscillation periods, to characterize the karst network. We describe in section 2 the experimental study site, the harmonic pumping investigation led on it, and the processing made on the measured field responses for the later interpretation. Then, in section 3 we briefly introduce the numerical model setup and the Cellular Automata-based Deterministic Inversion (CADI) algorithm. Further details of our inverse algorithm can be found in Fischer et al. (2017b). In section 4 we present the inversion results obtained with the CADI method at the Terrieu field site and the efficiency of the method in reproducing the

observed hydraulic responses. Finally, section 5 presents a discussion of the effect of the harmonic signal period on the inversion results.

2. Field investigation

2.1. Experimental site presentation

The Terrieu experimental site is located ~15 km in north of the town of Montpellier in southern France. The site consists of 22 vertical boreholes drilled within a surface area of approximately 2,500 m² (40 m × 60 m) and permits the study of karstic flows at a local scale (Figure 1). As a part of the network of the French Karst Observatory (SNO Karst, *www.sokarst.org*) and the Medycyss network (Jourde et al. 2011), the site has been used as a field laboratory for testing new field hydraulic methods and tools developed for the characterization of karstic aquifers (Jourde et al. 2002; Jazayeri Noushabadi 2009; Jazayeri Noushabadi et al. 2011; Dausse 2015; Wang et al. 2016; Wang et al. 2017; Fischer et al. 2017c).

The geological logs collected from the different boreholes shows that the subsurface of the field is composed of 35 to 45 m of thin-layered marly Cretaceous limestones, deposited on pure and massive Jurassic limestones. The interface between these two units is a sloped monocline bedding plane dipping at 20° toward Nord-West (Wang et al. 2016).

The Terrieu field is located in the Lez regional aquifer. Temperature and electrical conductivity measurements, and packer tests in boreholes presented in previous works (Jazayeri Noushabadi 2009; Dausse 2015) have shown the existence of preferential flow paths (shown in Figure 1) along the bedding plane between the Cretaceous and Jurassic limestones. Downhole videos in the boreholes show, that, at this interface, karstic conduits with aperture up to 50 cm are present (Jazayeri Noushabadi et al. 2011).

The massive Jurassic limestones are non-aquifer and the Cretaceous limestones have a low permeability. This causes the aquifer to be confined at the interface between these two layers, in the bedding plane. A network of karstic conduits has developed preferentially on this bedding plane, and controls the fluid circulation within the aquifer.

2.2.Harmonic pumping investigation

The main dataset used in this study was collected from an investigation using harmonic pumping tests performed at the Terrieu site. We have conducted pumping sequentially in four different boreholes while recording the water-level responses in 13 selected observational boreholes (see Figure 1). The water-level responses were also measured in the pumping wells P9, P15 and P20 but not in P3.

The static water level before the hydraulic investigation was at a depth of 20 m. The maximal drawdown generated by the pumping tests was 4 m. Therefore the karstic conduits (located at a depth of 35 to 45 m) were saturated during the entire duration of hydraulic tests.

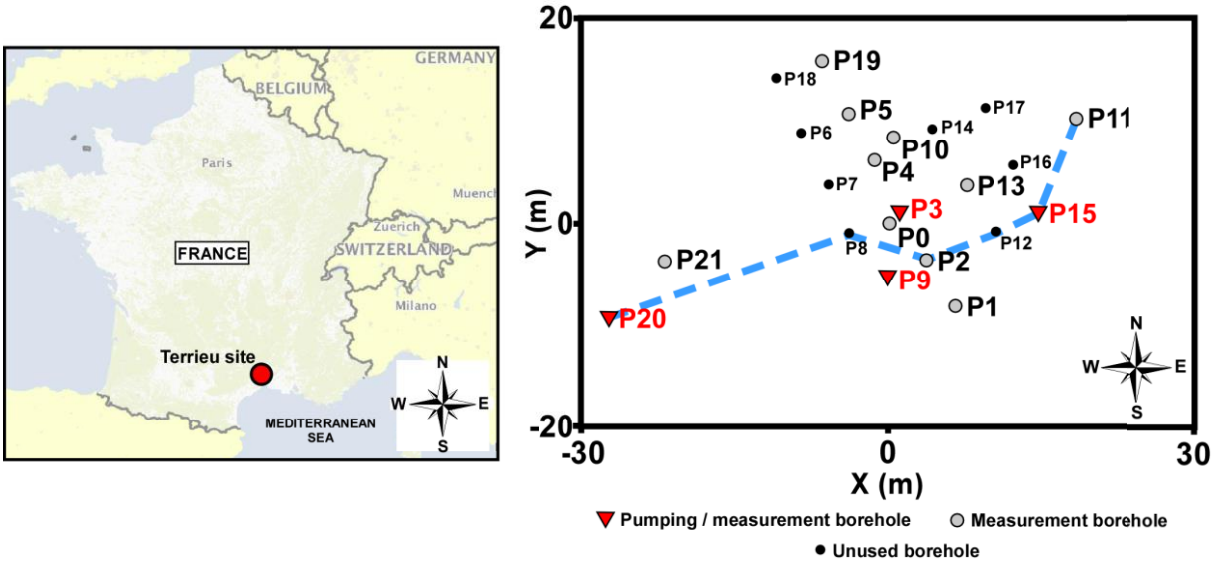

Figure 1: Maps of localization of the Terrieu site in France (left) and well pattern on the site (right). Boreholes used as pumping and measurement points are indicated using red triangles, and boreholes used only as measurement points are indicated using grey circles. Boreholes indicated by solid black points were not used during the investigation. The blue dotted line

delineates a preferential flow path identified by previous studies (Jazayeri Noushabadi 2009 and Dausse 2015), which shows a connectivity between P2, P8, P11, P12, P15 and P20.

The harmonic pumping tests were performed with a configurable electronical device, specially designed for this study by electronics engineers. This device controls a flow rate variator linked to the pump, which can generate a pumping signal with a sinusoidal shape around a mean value. The period and amplitude of the sinusoid signal can be configured with the device. The generated pumping rate can be described by:

$$Q(t) = Q_m - Q_A \cos(\omega t) \quad , \tag{1}$$

where Q is the output pumping signal (m^3/s), Q_m the mean pumping rate (m^3/s), Q_A the oscillatory signal amplitude (m^3/s), and $\omega = \frac{2\pi}{T}$ the pulsation ($rad.s^{-1}$) with T the period (s).

Different signal amplitudes and mean values were independently applied in each different pumping borehole according to its productivity (see Table 1).

Table 1: Harmonic pumping rates registered for each pumping point during the investigation. Q_A and Q_m refer to Eq. 1.

Pumping well:		**P3**	**P9**	**P15**	**P20**
Pumping rate (m^3/h)	**Amp. Q_A**	1	0.22	2.1	2.5
	Mean Q_m	4.1	0.35	5.3	3.8

For each pumping location, two pumping tests with different periods ($T = 2$ min and $T = 5$ min) were conducted during 30 min (15 cycles for a 2 min period, 6 cycles for a 5 min period). Water-level variations were continuously measured with digital pressure sensors installed in the measurement wells.

Overall, this investigation permitted to record 104 drawdown curves (13 measurements for each 2 different periods of signal applied in each 4 pumping wells).

2.3. Data processing

In order to interpret the harmonic signal in the drawdown curves, we have performed the same signal decomposition as proposed in Fischer et al. (2018b). This decomposition consists in removing the linear part, induced by the mean pumping signal Q_m, from the drawdown curve (through a linear regression) to keep only the oscillatory response. This operation is feasible only after an early transient period (accordingly we truncate the first cycle of the recorded responses). As we show in Figure 2 for the pumping in P15, the operation of removing the linear part is acceptable, as the resulting signals appear to be purely oscillatory. Some natural noises and vibrations induced by the pumping appear as high frequencies fluctuations in the oscillatory responses.

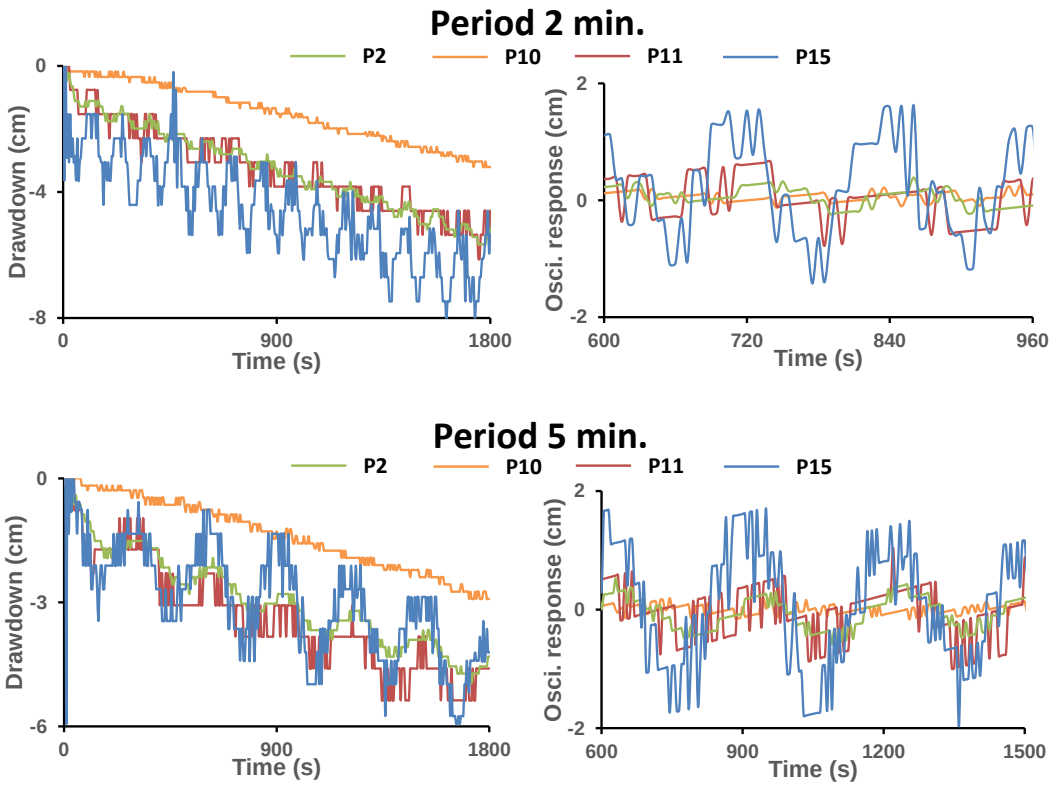

192

193 Figure 2: Left: Measured drawdown curves for a selection of boreholes (P2, P10, P11, P15)
194 during a pumping in P15 with a 2 min and a 5 min period. Right: Zoom-in view of three
195 oscillation cycles after removing the linear part from the drawdown curves.

196

197 Mathematically the drawdown curves generated by the harmonic pumping tests can be
198 approximated as a sum of a linear signal and an oscillatory signal applied on the initial water
199 table level:

200
$$h(t) \simeq h_{lin.}(t) + h_{osc.}(t) + H_0$$
$$\text{with} \quad h_{lin.}(t) \simeq -at - h_0 \quad \text{and} \quad h_{osc.}(t) \simeq A\cos\left(\frac{2\pi}{T}t - \Phi\frac{\pi}{180}\right) \qquad (2)$$

201 where h represents the drawdown (m) over time, $h_{lin.}$ is a linear signal described by its slope a
202 (m/s) and its intercept h_0 (m) (whose values can be retrieved by linear regression), $h_{osc.}$ is an
203 oscillatory signal described by its amplitude A (m), its period T (s) and its phase shift Φ (°),
204 and H_0 represents the initial water table level (m) (in our case we considered $H_0 = 0$ m).

The linear signal $h_{lin.}$ can be easily estimated in a first approximation through a linear regression performed on each drawdown curve. After removing this linear trend, the amplitude and phase offset of the remaining signal of each borehole can be determined by a Fast Fourier Transform (FFT) on their oscillatory signals. The FFT permits to extract the main oscillatory components of a signal, to denoise it, and to interpret its parameters. Figure 3 presents the FFT results for the oscillatory signals of three representative boreholes (P10, P11, P2) during a pumping in P15 with the two periods (2 min and 5 min). The interpretation results of amplitude and phase offset for the entire dataset are presented in Appendix 1.

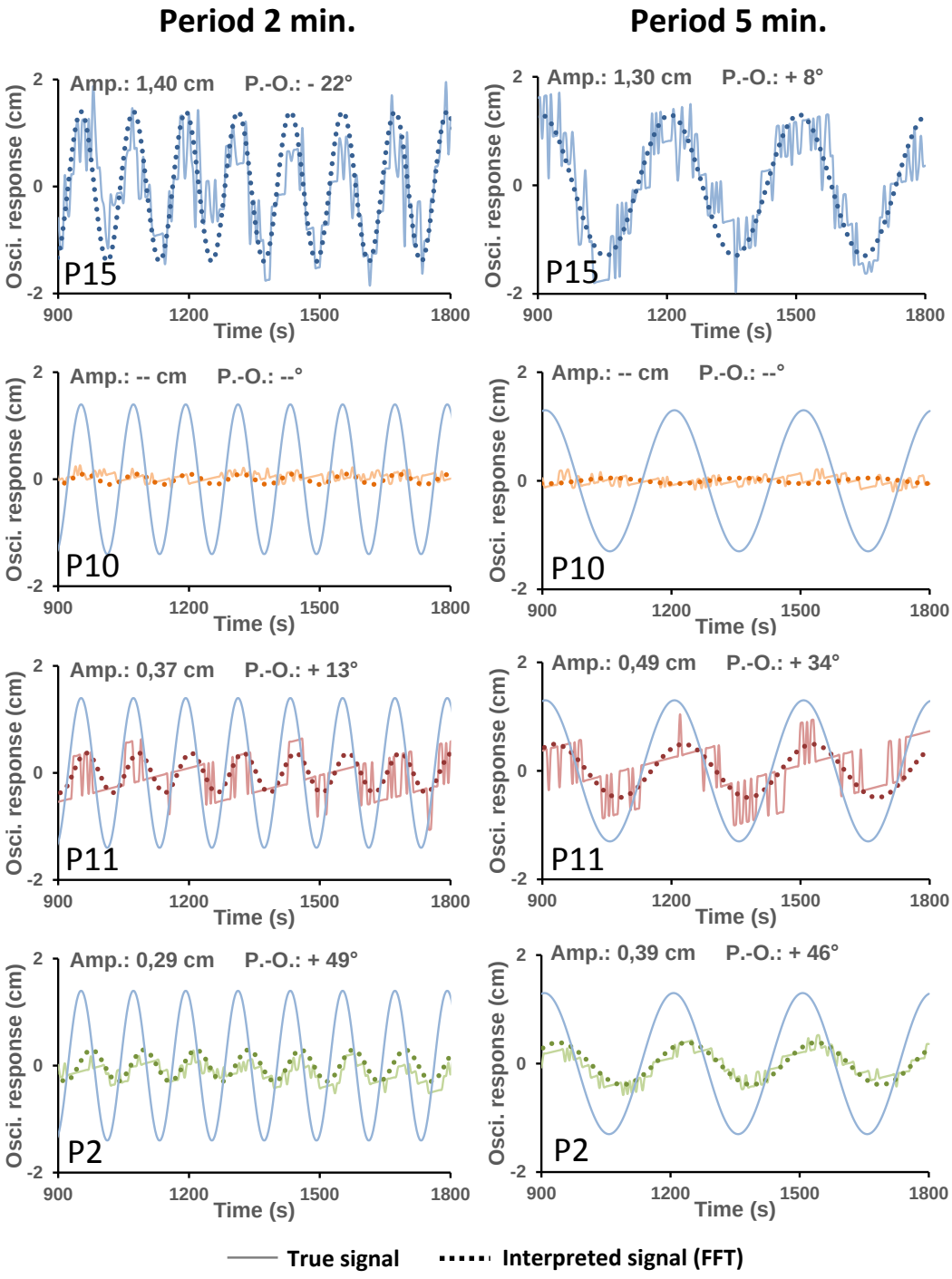

213

214 Figure 3: Zoom-in on the oscillatory responses extracted from the drawdown measured in P2,
215 P10, P11 and P15 during pumping tests in P15 with a 2 min (left) and a 5 min (right) signal
216 periods and FFT results of the interpreted amplitude (Amp.) and phase offset (P.-O.)
217 responses. Solid lines represent the measured signals, dotted lines represent the interpreted
218 signals ($h_{osc.}$ in Eq. 2) reconstructed from the amplitudes and phase offsets interpreted by
219 FFT. For interpreted amplitudes smaller than 1 mm (for example here in P10), we considered
220 the oscillatory responses to be negligible. The blue lines represent the interpreted pumping
221 signals (P15) and are presented for each borehole for a better visualization of the interpreted
222 phase offset responses.

2.4. Preliminary analysis

The different responses of amplitude and phase offset interpreted in P10, P11 and P2 highlight three distinct flow behaviors (Fischer et al. 2018b). The responses in P10, having a negligible amplitude (< 1 mm) relatively to the pumping signal, which we interpreted as a negligible oscillatory response, is associated to a 'matrix connectivity' between the pumping and the observational well. In contrast, the response in P11 has a significant amplitude and an almost invariable phase relatively to the pumping signal for the two different periods. This behavior is associated to a 'conduit connectivity' response, meaning that P15 and P11 would be connected through a karstic conduit network. The response in P2 has a lower amplitude response than P11, and its phase offset relatively to the pumping signal increases as the pumping period decreases (+71 ° for a 2 min signal, +38 ° for a 5 min signal). This third behavior is associated to a 'dual connectivity' response, which corresponds to an inter-well connection either through fissures or when the observation borehole is located in the matrix but close to a conduit.

Following the method described in Fischer et al. (2018b) and through the integration of the amplitude and phase offset results interpreted for each pumping-observation well pair, it is possible to obtain a map of inter-well connectivity which contains qualitative information regarding the spatial distribution of the conduit network and the relative position of boreholes to the network. We can first link, on the map, the boreholes with a low phase shift relatively to the pumping signal, to represent a conduit connection. From this conduit connectivity we can then establish a possible conduit network, and then verify that the other boreholes responses would be adequate toward their position to the interpret network (dual connectivity with higher phase shift for boreholes close to the network and matrix connectivity with negligible responses for the others).

Possible connectivity maps interpreted with the responses to the harmonic pumping test in P15 for a period of 2 min. and 5 min. are proposed in Figure 4.

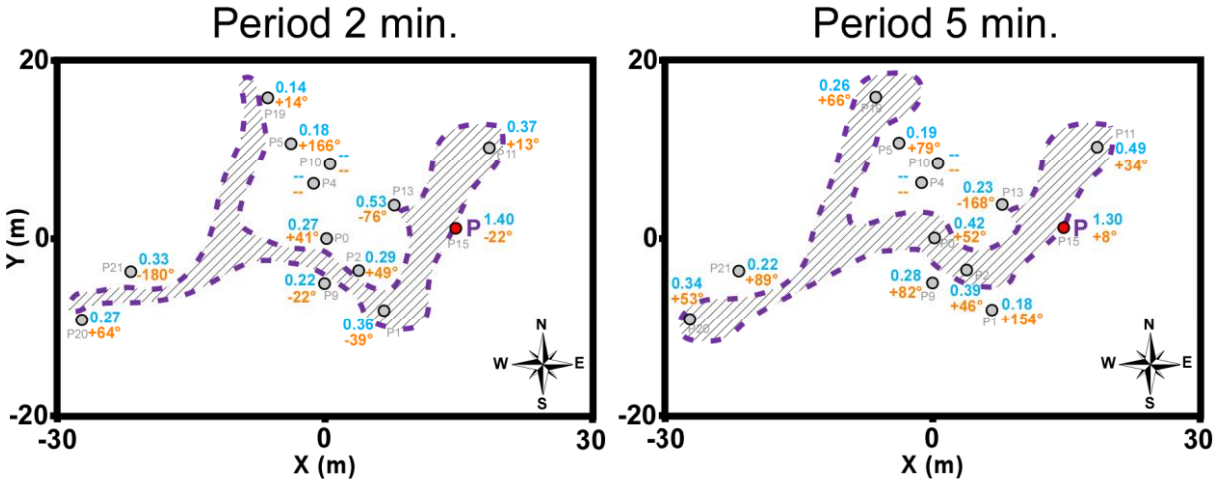

Figure 4: Connectivity maps interpreted from the amplitude (in blue) and phase offset (in orange) responses to a pumping in P15 with a 2 min (left) and a 5 min (right) period of signal. The areas within the dotted lines delineate a possible area where boreholes are connected through a direct conduit connectivity. Dashes indicate negligible oscillatory responses.

The comparison between the two connectivity maps in Figure 4 shows that the period of the harmonic pumping signal may have a slight impact on the connectivity interpretation. For example in the pumping test with a 2 min period P1 can be interpreted as connected to the pumping well through conduits, but not in the pumping test with a 5 min period. This implies that a change in the period of the pumping signal modifies the flow field induced by the pumping.

Furthermore, the manual interpretation is possible only when the amount of hydraulic data to deal with is limited (13 responses for each period in Figure 4). Therefore, although such a qualitative analysis through manual interpretation of inter-well connectivity could provide some important guidance to hydrogeological investigation, such as indicating the general trend of the main conduits and relative inter-well connectivity, to obtain a quantitative hydrodynamics characterization and to integrate a larger amount of hydraulic measurements

(104 responses from 4 different pumping locations with each time two different periods) an inverse modelling is required.

3. Modeling methodology

3.1. Forward problem and model parameterization

Inverse modeling involves the use of the forward problem in order to simulate, for a given model of hydraulic properties, the hydraulic responses. In this section we present a 2D model that represents the property field along the bedding plane interface, in which the karstic network has developed on the Terrieu site.

As seen in the previous section, the variation of the piezometric level among the site, in response to a harmonic pumping, can be approximated by the sum of a linear drawdown and an oscillatory drawdown (Eq. 2). We simulate in the model only the oscillatory part of the drawdown responses $h_{osc.}$. The inversion aims to reproduce the values of amplitude and phase offset of the oscillatory part in the measured responses. This oscillatory part can be described as a signal in the frequency domain in the model:

$$h_{osc.}(x,y,t) = Re\left(\mathcal{H}_{\omega}(x,y)e^{i\omega t}\right) . \quad (3)$$

with $\mathcal{H}_{\omega}$ a complex parameter holding the amplitude and phase offset responses over space (x,y), Re the function returning the real part of a complex value, $\omega = \frac{2\pi}{T}$ the pulsation (rad.s^{-1}) and i the imaginary unit.

This oscillatory feature of the hydraulic signal permits to rewrite the time domain form of the groundwater flow equation into a frequency form, in order to reduce the computation time of the forward problem.

In a 2D, porous, isotropic and saturated domain $\mathbf{\Gamma}$ the groundwater flow equation based on the Darcy's law in a frequency domain can be expressed as:

$$i\omega S_S \mathcal{H}_\omega - \nabla \cdot \left(K . \nabla \mathcal{H}_\omega \right) = \frac{Q_A}{\mathcal{V}_{el.}} \delta \left(x - x_s, y - y_s \right) , \quad (4)$$

with S_S the specific storage distribution (m^{-1}), K the conductivity distribution (m/s), Q_A the pumping amplitude (m3/s), $\mathcal{V}_{el.}$ an elementary volume of the finite element grid in the model, and $\delta(x - x_s, y - y_s)$ the Dirac distribution where x_s, y_s represents a pumping location. As the system is 2D, with a unit thickness, conductivity K and transmissivity T are of same value, as well as specific storage S_S and storativity S. In this study we considered the Darcy's law to be acceptable for representing the flows generated in the karstic structures. In fact, it appears from the previous studies on the Terrieu site that the flows in the conduits have a low velocity, inducing a low Reynolds value, even for higher pumping rates than the ones used during this new investigation.

The initial and boundary conditions used for solving Eq. 4 are:

$$\begin{array}{l} \mathcal{H}_\omega (x, y) = 0 \quad \forall (x, y) \in \mathbf{\Gamma} \text{ as initial condition} \\ \mathcal{H}_\omega (x, y) = 0 \quad \text{when } (x, y) \in \mathbf{\Gamma}_{bound.} \text{ as boundary condition} \end{array} . \quad (5)$$

The spatial distribution of the complex parameter $\mathcal{H}_\omega$ permits the reconstruction of the oscillatory responses simulated among the model, through the calculation of their amplitude and phase offset values:

$$\left| \begin{array}{ll} - \textit{Amplitude}: & A(x, y) = \sqrt{\left(Re\, \mathcal{H}_\omega (x, y) \right)^2 + \left(Im\, \mathcal{H}_\omega (x, y) \right)^2} \quad \text{in m} \\ - \textit{Phase offset}: & \Phi(x, y) = \frac{180}{\pi} atan2\left(-Im\, \mathcal{H}_\omega (x, y), Re\, \mathcal{H}_\omega (x, y) \right) \text{ in } ^\circ \end{array} \right. , \quad (6)$$

where *Re* and *Im* are the functions returning the real and imaginary parts of a complex value, and *atan2* is the function returning the inverse tangent value in radian mode from two arguments.

The simulated response signals are then reconstructed temporally and spatially:

$$h_{osc.}(x,y,t) = A(x,y)\cos\left(\omega t - \Phi(x,y)\frac{\pi}{180}\right) . \quad (7)$$

In a karstic medium, the spatial response signals are very dependent to the highly heterogeneous distribution of the field properties T and S along the karstic conduits. Therefore this heterogeneity has to be taken into account in the distribution of these properties in the model in order to simulate a realistic responses behavior. For this purpose we chose to apply as parameterization for our model and inverse problem the Cellular Automata-based Deterministic Inversion (CADI) method, developed and detailed in Fischer et al. (2017b). For a detailed description of the CADI method we refer the reader to Fischer et al. (2017b), as we will only briefly summarize the concept in this article.

The CADI method uses a particular parameterization of the property field in the model to generate linear structures (conduits) over a background (matrix). The field is composed of a grid of cells, each cell being assigned to a value of transmissivity and storativity. This grid of cells is divided in m_{CA} subspaces, each one being controlled by a cellular automaton piloting the part of the cells inside of its subspace (Figure 5). The cellular automata concept is a mathematical tool which permits to generate structures within a grid with simple neighborhood and transition rules (Von Neumann and Burks 1966). The cellular automata control the local direction of generation of the conduit in the different subspaces. They are piloted through eight different neighborhood definition $N_i, i \in [1,8]$ that permit to define eight different directions. One of these eight direction possibilities is assigned to each cellular

automaton in the subspaces. The conduit network is generated by first assigning a state ‘matrix’ or ‘conduit’ to each cell. The whole cells are initially in state ‘matrix’, except an initial cell of the grid in state ‘conduit’ which designates the starting point and starting subspace for the generation of the conduits. The network of conduits then generates following the different local direction affected to each subspace it crosses. The generation ends once each part of the network has reached an end (either the limit of the model or a subspace in which the network has already generated).

Then property values are assigned to the cells depending on their state (‘matrix’ or ‘conduit’) and their localization (subspace). Each subspace defines locally a value for T_{mat} and S_{mat} for its cells in state ‘matrix’ and a value for T_{cond} and S_{cond} for its cells in state ‘conduit’.

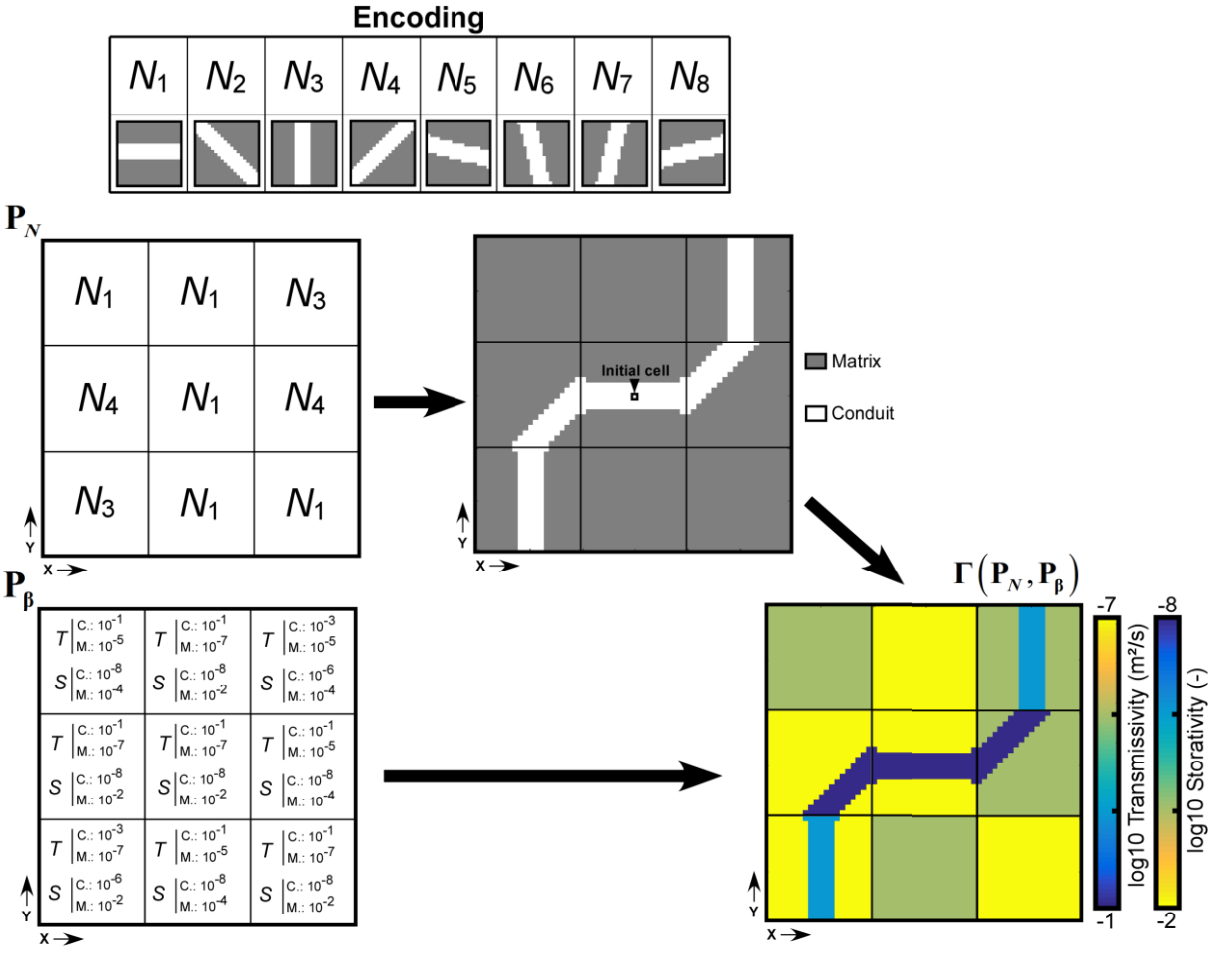

Figure 5: Schema of the parameterization of a model with the CADI method. $\mathbf{P}_N$ contains the encoded (see Encoding) structural directions of generation associated to each subspace which permits to generate, from an initial 'conduit' cell, a network of conduits in the matrix. $\mathbf{P}_\beta$ contains the conduit (C) and matrix (M) transmissivity and storativity values associated to each subspace. $\mathbf{\Gamma}\left(\mathbf{P}_N, \mathbf{P}_\beta\right)$ designates the model produced by applying the property values from $\mathbf{P}_\beta$ to the network generated from $\mathbf{P}_N$.

In order to be able to easily pilot and modify the configuration of the model through this parameterization, the structural directions and properties assigned to each subspace are defined in two parameter vectors: $\mathbf{P}_N$ and $\mathbf{P}_\beta$. $\mathbf{P}_N$ is a m_{CA}-vector containing the directions of generation $N_i, i \in [1,8]$ assigned to each subspace. Several independent networks can be generated in the same model with different directions parameters for each network. In this case $\mathbf{P}_N$ becomes a $(m_{\mathrm{CA}} \times frac)$ matrix where $frac$ represents the amount of independent

networks in the model. Each column contains the subspaces directions for each network. $\mathbf{P}_{\beta}$ is a $4m_{\mathrm{CA}}$-vector containing the T_{mat} and S_{mat} and the T_{cond} and S_{cond} values assigned to each subspace. In this way the parameters controlling the configuration of the model, and thus the model itself, can be easily and locally modified. $\mathbf{P}_{N}$ and $\mathbf{P}_{\beta}$ represent the parameters to be optimized in the inverse problem in order to reproduce the observed data (amplitude and phase offset responses) through a suitable model.

3.2. Inverse problem

The inverse problem consists in retrieving the best values for the parameters contained in $\mathbf{P}_{N}$ and $\mathbf{P}_{\beta}$ regarding the minimization of the gap between the simulated data and the observed data (amplitude and phase offset responses at the measurement points for the different pumping tests). This inverse algorithm contains two steps in which we seek to minimize two objective functions sequentially, $\Psi_{\mathrm{structure}}$ for the optimization of the structural parameter $\mathbf{P}_{N}$ and $\Psi_{\mathrm{properties}}$ for the optimization of the property parameter $\mathbf{P}_{\beta}$ (Tarantola and Valette 1982):

$$\Psi_{\mathrm{structure}}\left(\mathbf{P}_{N}\right)=\frac{1}{2}\left(\mathbf{d}_{\mathrm{obs}}-f\left(\boldsymbol{\Gamma}\left(\mathbf{P}_{N},\mathbf{P}_{\beta}\right)\right)\right)^{\mathrm{T}}\mathbf{C}_{\mathbf{d}}{}^{-1}\left(\mathbf{d}_{\mathrm{obs}}-f\left(\boldsymbol{\Gamma}\left(\mathbf{P}_{N},\mathbf{P}_{\beta}\right)\right)\right)+\frac{1}{2}\left(\mathbf{P}_{N,\mathrm{prior}}-\mathbf{P}_{N}\right)^{\mathrm{T}}\mathbf{C}_{\mathbf{P}_{N}}{}^{-1}\left(\mathbf{P}_{N,\mathrm{prior}}-\mathbf{P}_{N}\right) \quad (8)$$

$$\Psi_{\mathrm{properties}}\left(\mathbf{P}_{\beta}\right)=\frac{1}{2}\left(\mathbf{d}_{\mathrm{obs}}-f\left(\boldsymbol{\Gamma}\left(\mathbf{P}_{N},\mathbf{P}_{\beta}\right)\right)\right)^{\mathrm{T}}\mathbf{C}_{\mathbf{d}}{}^{-1}\left(\mathbf{d}_{\mathrm{obs}}-f\left(\boldsymbol{\Gamma}\left(\mathbf{P}_{N},\mathbf{P}_{\beta}\right)\right)\right)+\frac{1}{2}\left(\mathbf{P}_{\beta,\mathrm{prior}}-\mathbf{P}_{\beta}\right)^{\mathrm{T}}\mathbf{C}_{\mathbf{P}_{\beta}}{}^{-1}\left(\mathbf{P}_{\beta,\mathrm{prior}}-\mathbf{P}_{\beta}\right) \quad (9)$$

where $\mathbf{d}_{\mathrm{obs}}$ is a n-vector containing the n measured responses, $f\left(\boldsymbol{\Gamma}\left(\mathbf{P}_{N},\mathbf{P}_{\beta}\right)\right)$ is a n-vector containing the responses simulated with the model at the same positions than in $\mathbf{d}_{\mathrm{obs}}$, $\mathbf{C}_{\mathbf{d}}$ is a $(n\times n)$ matrix of covariance on the data, $\mathbf{P}_{N,\mathrm{prior}}$ is a m_{CA}-vector holding *a priori*

structural parameters for $\mathbf{P}_{\boldsymbol{N}}$, $\mathbf{P}_{\boldsymbol{\beta},\text{prior}}$ is a $4m_{\text{CA}}$-vector holding *a priori* property values for $\mathbf{P}_{\boldsymbol{\beta}}$, and $\mathbf{C}_{\mathbf{P}_{\boldsymbol{N}}}$ and $\mathbf{C}_{\mathbf{P}_{\boldsymbol{\beta}}}$ are $(m_{\text{CA}} \times m_{\text{CA}})$ and $(4m_{\text{CA}} \times 4m_{\text{CA}})$ matrices of prior covariance on the parameters $\mathbf{P}_{\boldsymbol{N}}$ and $\mathbf{P}_{\boldsymbol{\beta}}$.

At the beginning of the inversion process, the variable parameters $\mathbf{P}_{\boldsymbol{N}}$ and $\mathbf{P}_{\boldsymbol{\beta}}$ are initialized with a priori conduit directions and property values in order to create the initial model. Then a sequential and deterministic process optimizes firstly the structural parameters in $\mathbf{P}_{\boldsymbol{N}}$ (considering the initial properties in $\mathbf{P}_{\boldsymbol{\beta}}$ as invariable), and then, in second step, the property parameters in $\mathbf{P}_{\boldsymbol{\beta}}$ (considering the previously optimized $\mathbf{P}_{\boldsymbol{N}}$ as invariable). Finally, after the optimization process, the posterior uncertainties on the structural and property parameters are estimated.

a. Optimization of the structural parameters:

The optimization of the structural parameters in $\mathbf{P}_{\boldsymbol{N}}$ is an iterative process in which a sensitivity matrix is computed, at each iteration step, to minimize the objective function in Eq. 8. This analysis requires the computation of a $(8 \times m_{\text{CA}})$ sensitivity matrix $\mathbf{S}$. At a given iteration step k, each element (i, j) of the matrix is calculated as follow:

$$\begin{aligned}\mathbf{S}^{\text{k}}(\text{i},\text{j}) = &\left(\mathbf{d}_{\text{obs}} - f\left(\boldsymbol{\Gamma}\left(\mathbf{P}_{\boldsymbol{N}}^{\text{k}}\big|_{\mathbf{P}_{\boldsymbol{N}}^{\text{k}}(\text{j})=N_{\text{i}}}, \mathbf{P}_{\boldsymbol{\beta}}\right)\right)\right)^{\text{T}} \mathbf{C}_{\mathbf{d}}{}^{-1}\left(\mathbf{d}_{\text{obs}} - f\left(\boldsymbol{\Gamma}\left(\mathbf{P}_{\boldsymbol{N}}^{\text{k}}\big|_{\mathbf{P}_{\boldsymbol{N}}^{\text{k}}(\text{j})=N_{\text{i}}}, \mathbf{P}_{\boldsymbol{\beta}}\right)\right)\right) \\ &+ \frac{1}{2}\left(\mathbf{P}_{\boldsymbol{N},\text{prior}}(\text{j}) - N_{\text{i}}\right)^{\text{T}} \mathbf{C}_{\mathbf{P}_{\boldsymbol{N}}}{}^{-1}\left(\mathbf{P}_{\boldsymbol{N},\text{prior}}(\text{j}) - N_{\text{i}}\right)\end{aligned} \tag{10}$$

where $f\left(\boldsymbol{\Gamma}\left(\mathbf{P}_{\boldsymbol{N}}^{\text{k}}\big|_{\mathbf{P}_{\boldsymbol{N}}^{\text{k}}(\text{j})=N_{\text{i}}}, \mathbf{P}_{\boldsymbol{\beta}}\right)\right)$ represents the responses simulated with the modified direction N_{i} in the subspace $\mathbf{P}_{\boldsymbol{N}}^{\text{k}}(\text{j})$, and $\mathbf{P}_{\boldsymbol{N},\text{prior}}(\text{j}) - N_{\text{i}}$ denotes the angular gap between the modified direction N_{i} and the *a priori* direction $\mathbf{P}_{\boldsymbol{N},\text{prior}}(\text{j})$.

The coordinates (i_{min}, j_{min}) of the minimal value in the sensitivity matrix provide the subspace to be optimized (j_{min}) and the direction to apply (i_{min}) in order to minimize the objective function during this iteration. At the end of an iteration, the value of the structural objective function is recalculated. This iterative optimization ends when the objective function has reached a minimum (no more structural modification can decrease the objective function). The optimized parameters in $\mathbf{P}_N$ will then be considered as invariable during the optimization of $\mathbf{P}_\beta$.

After the convergence of the objective function in the structural optimization, the uncertainties on the local directions of the geometry of the network can be estimated from the posterior structural covariance:

$$\mathbf{C}_{\mathbf{P}_N}^{post}(j) = \left(\frac{1}{8} \sum_{i=1}^{8} \mathbf{S}^{post}(i,j) - \Psi_{structure}^{post} + \mathbf{C}_{\mathbf{P}_N}{}^{-1}(j,j) \right)^{-1} \quad (11)$$

where $\mathbf{C}_{\mathbf{P}_N}^{post}(j)$ denotes the uncertainty associated to the direction of the subspace j, $\mathbf{S}^{post}$ is the sensitivity matrix of the last iteration, and $\Psi_{structure}^{post}$ is the value of the minimized objective function associated to the last iteration. The higher the uncertainty value associated to a subspace is, the more the direction of the subspace in uncertain. In the contrary a low value denotes a well constrained direction.

b. Optimization of the property parameters

In the second step, we estimate the hydraulic properties in $\mathbf{P}_\beta$ through an iterative optimization process and by considering the previously optimized $\mathbf{P}_N$ as invariable. The process relies on a linearization of the objective function in Eq. 9, through the computation of

411 the Jacobian matrix. At an iteration step k, the values of the properties in $\mathbf{P}_{\beta}$ are updated from
412 the previous ones as follow:

413
$$\mathbf{P}_{\beta}^{k+1} = \mathbf{P}_{\beta}^{k} + \left(\left(\mathbf{J}^{k}\right)^{T}.\mathbf{C}_{\mathbf{d}}{}^{-1}.\mathbf{J}^{k} + \mathbf{C}_{\mathbf{P}_{\beta}}{}^{-1}\right)^{-1}.\left(\mathbf{J}^{k}\right)^{T}.\mathbf{C}_{\mathbf{d}}{}^{-1}.\left(\mathbf{d}_{\text{obs}} - f\left(\mathbf{\Gamma}\left(\mathbf{P}_{N}, \mathbf{P}_{\beta}^{k}\right)\right)\right) + \mathbf{C}_{\mathbf{P}_{\beta}}{}^{-1}.\left(\mathbf{P}_{\beta,\text{prior}} - \mathbf{P}_{\beta}^{k}\right) \quad (12)$$

414 where $\mathbf{J}$ is the $(n \times 4m_{\text{CA}})$ Jacobian matrix calculated with a finite difference method:

415 $\mathbf{J}(\text{i}, \text{j}) = \left.\dfrac{\partial f_{\text{i}}}{\partial \mathbf{P}_{\beta}}\right|_{\mathbf{P}_{\beta}(\text{j})=\mathbf{P}_{\beta}(\text{j})+\Delta\mathbf{P}_{\beta}}$ with $\Delta\mathbf{P}_{\beta}$ a finite difference step.

416 The value of the properties objective function is recalculated at the end of each iteration. This
417 iterative optimization ends when the objective function converges to a minimum value.

418 The uncertainties on the T and S values can then be estimated through the computation of
419 the posterior properties covariance matrix. The square root values of the diagonal entries of
420 this matrix represent the standard deviation associated to each property value:

421
$$\mathbf{C}_{\mathbf{P}_{\beta}}^{post} = \left(\left(\mathbf{J}^{post}\right)^{T}.\mathbf{C}_{\mathbf{d}}{}^{-1}.\mathbf{J}^{post} + \mathbf{C}_{\mathbf{P}_{\beta}}{}^{-1}\right)^{-1} \quad (13)$$

422 where $\mathbf{C}_{\mathbf{P}_{\beta}}^{post}(\text{j}, \text{j})$ denotes the variance of the j^{th} property parameter in $\mathbf{P}_{\beta}$, and $\mathbf{J}^{post}$ is the
423 Jacobian matrix of the last iteration.

424 # 4. Modeling application

425 ## 4.1. Modeling strategy

426 We have applied the CADI method on the 2D parameterized model presented in the previous
427 section, in order to find a structured property distribution able to reproduce the measured
428 oscillatory responses (amplitudes and phase offsets) presented in the section 2.3. We
429 considered the oscillatory responses interpreted as negligible (amplitude < 1 mm) to be null

for the inversion. We have coded the CADI algorithm with Matlab and used Comsol Multiphysics to solve the model in the frequency domain (see Eq. 5). This resolution was led using a finite element method on a triangular mesh, refined around the boundaries between the matrix and the conduit network represented by the equivalent porous media properties distributed over the model. This mesh refinement is performed with the Comsol *mphimage2geom* function on the conduit network image generated by the cellular automata.

The distributed model is constructed as a 40×60 m² rectangle included in a $1{,}000 \times 1{,}000$ m² buffer zone. The external boundaries of the buffer zone are built with imposed Dirichlet boundary conditions as presented in Eq. 5. Thus, this zone permits to limit the effect of the boundary conditions on the parameterized model.

The values of the parameters chosen for the model parametrization and the inversion process are presented in Table 2. The initial values for the inversion were chosen accordingly to estimates from previous studies on the Terrieu site (Jazayeri Noushabadi 2009 ; Dausse 2015 ; Wang et al. 2016). In the inverse problem the properties values β in $\mathbf{P}_\beta$ were associated to the exponent of the transmissivity and the storativity. The initial standard deviation values on the data (σ_{data}) and on the property parameters (σ_T , σ_S) are used to construct the covariance matrices as diagonal matrices: $\mathbf{C_d} = {\sigma_{\text{data}}}^2 \times Id(n)$ and $\mathbf{C}_{\mathbf{P}_\beta} = {\sigma_{\text{prop.}}}^2 \times Id(4m_{\text{CA}})$. No *a priori* information were considered for the structure local directions in $\mathbf{P}_{N,\text{prior}}$ and $\mathbf{C}_{\mathbf{P}_N}$.

Table 2: Parameters used for the inversion process.

Parameter	Value
Final partitioning	12×8
Final grid size	Δx : 0.25 m ; Δy : 0.25 m
Final network thickness	1 m
T_{init}	10^{-1} m²/s for the conduits ; 10^{-6} m²/s for the matrix
S_{init}	10^{-8} for the conduits ; 10^{-4} for the matrix
T_{buffer} ; S_{buffer}	10^{-2} m²/s ; 10^{-3}

σ_{data}^2	0.01 on amplitude values 10 on phase offset values
$\sigma_{prop.}^2$	0.1 (applied on the exponent: $10^{\beta \pm \sigma_{prop}}$)

449

450 The inversion was led following a multi-scale method (Grimstadt et al. 2003), as described in
451 Figure 6. The multi-scale inversion consists in performing an inversion first for a coarse
452 resolution of the model, and then use the inversion result as a new initial model with a higher
453 resolution for a new inversion process. This permits to progressively reduce the size of the
454 discretization cells for the property field during the inversion, which can be interesting for
455 studies on heterogeneous fields with no prior information on the property distribution. This
456 was already done with the CADI method in Fischer et al. (2017c).

457 The initial model has been constructed with two unidirectional conduits with uniform
458 property values (see Table 2) as a coarse approximation of the manual estimation made in
459 Figure 4.

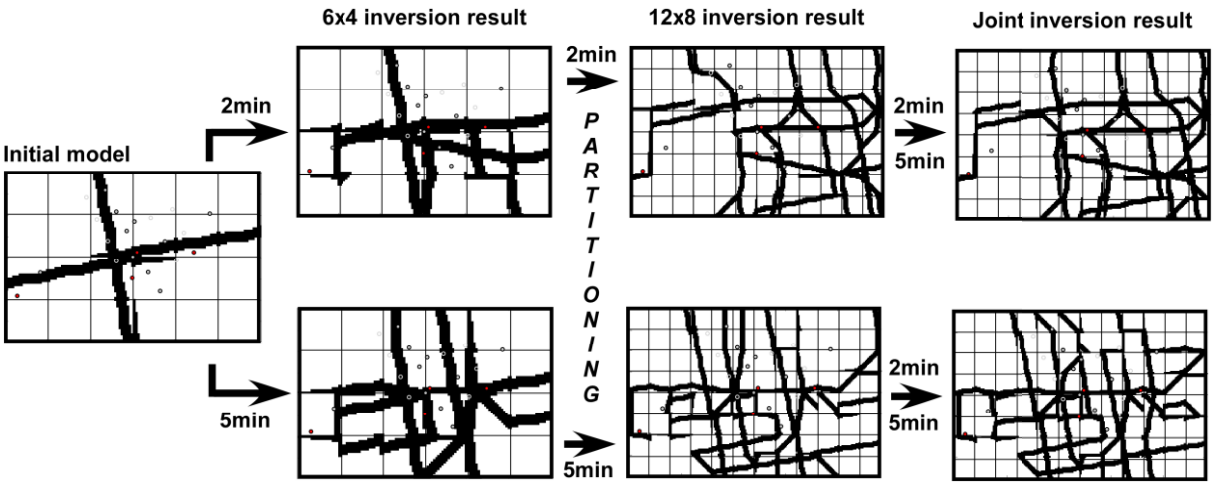

460

461 Figure 6: Schematization of the complete multi-scale inversion process. Starting from an
462 initial model, firsts inversions were led for a 6×4 partitioning (shown by the grid). The
463 results were refined to 12×8 subspaces and used for new inversions. Finally, joint inversion
464 were led starting from the results of the previous separate inversion.

465

A first set of inversions were led by separating the 2 min and 5 min period responses, and with a 6×4 subspaces partitioning of the model (with a conduit thickness of 2 m). The results of these separate inversions have then been repartitioned in 12×8 subspaces models (with a conduit thickness of 1 m), which were used as initial models for a new inversions with the same datasets. This partitioning of the models permits to give more liberty to the inversion process, while starting from 'not too far' solutions, which is especially interesting for a deterministic process. The inversion results for the 12×8 models with 2 min and 5 min data separated will be presented in section 4.2.

A final inversion process has consisted in starting from these 12×8 separate results, with the same partitioning, by adding the 5 min data to the 2 min inversion result and the 2 min data to the 5 min results, for joint inversions. The results of these joint inversions will be discussed in section 4.3.

4.2.Modeling results

Figure 9 shows the spatial distribution of hydraulic transmissivity and storativity inverted using the responses to the 2 min and 5 min periods, respectively. The comparison between the measured and simulated hydraulic responses is presented in Figure 7 and Table 3. It can be seen that the simulated responses match the measured ones quite well.

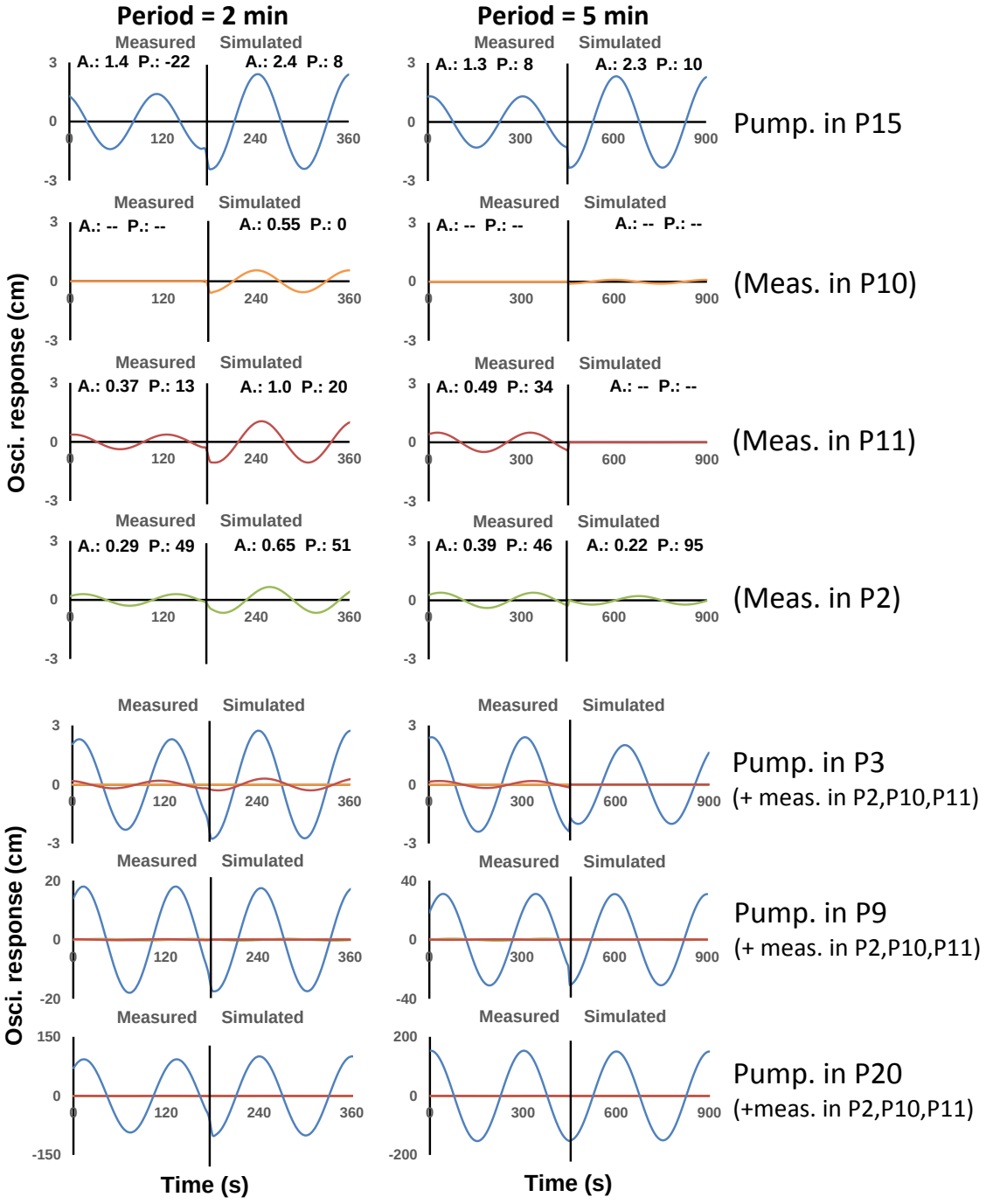

Figure 7: Comparison of some measured and simulated (with the property distributions presented in Figure 9) responses signals in observation points P2 (green), P10 (orange), P11 (red) and pumping points P3, P9, P15, P20 (each time in blue), for pumping signals with a 2 min (left) and a 5 min (right) period. In the case of the pumping in P3 we present in blue the signal in P0, located 1 m away from P3 (which was not measured during the investigation). For a better readability the responses are presented separately for a pumping in P15 with their amplitude (A. in cm) and their phase offset (P. in °) values. For the pumping in P3, P9 and P20 the responses are presented on a same graph.

493 The simulated responses to the P15 pumping appear to be slightly overestimated implying the
494 existence of a very productive conduit in P15 that could not be simulated in the presented
495 model. Otherwise, the responses proportions and behaviors for each pumping are well
496 respected with the simulated signals. Overall, the Root Mean Square Error (RMSE) of the
497 amplitude is 1.1 cm for the 2 min response signals, and 0.5 cm for the 5 min response signals.
498 The RMSE of the phase offset is 56 ° for the 2 min response signals, and 66 ° for the 5 min
499 response signals (see Table 3). The difficulties in reproducing the phase offset data with the
500 CADI method may be contributed to the high degree of variation of the phase shift within the
501 low transmissivity matrix (Figure 8). A small displacement of a certain wellbore location by 1
502 m in the matrix can modify the phase offset by a value of 90 °. Thus, our phase offset RMSEs
503 remain under the variations produced by a 1 m displacement on the field, which is acceptable
504 at our scale.

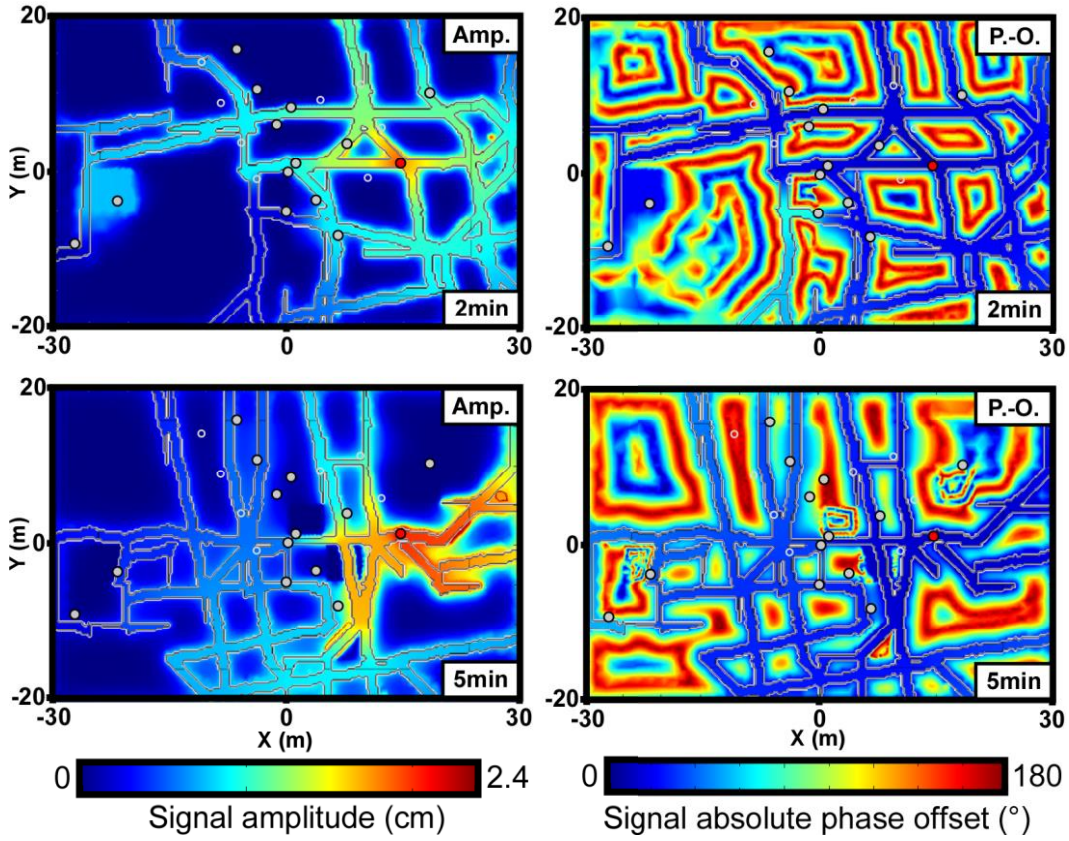

505

506 Figure 8: Maps of simulated spatial amplitude (Amp.) and phase offset (P.-O.) with the
507 models in Figure 9 for a pumping in P15 with a signal period of 2 min and 5 min.

508

509 The amplitude of the signal is also decaying very fast in the matrix (Figure 8), thus the
510 amplitude of a response is already a good information to characterize the proximity of a
511 borehole with a conduit of the karst network. According to Fischer et al. (2018b) and the
512 maps in Figure 8 produced with the CADI method, the amplitude in the responses signals of a
513 karstic aquifer permit to distinguish the boreholes in (or near) conduits from the ones in the
514 matrix. On the other side, the phase offset response permit to characterize more precisely the
515 distance of a responding borehole to conduits, as it varies orthogonally to the direction of the
516 conduit and stays very low within the network.

517 One advantage of using the CADI method in this work is that the optimized conduits
518 networks can be clearly distinguished from the matrix in the inverted fields in Figure 9. If

519 these optimized conduits networks represent only one possible geometry among other likely
520 models, they permit to interpret the relative positioning of each borehole (in a conduit, close
521 to a conduit, or in the matrix) and thus a degree of connectivity between them. The models of
522 networks produced by inversions of pumping tests of different periods are very different,
523 indicating that the both sets of responses provide different hydraulic information of the
524 aquifer. The reconstructed network for the dataset of a period of 5 min is denser than that for a
525 period of 2 min. The 5 min period dataset seems to carry information about karstic structures
526 of different scales (conduits, fractures, fissures) around the measurement points, while the 2
527 min period dataset tends to characterize more specifically the most conductive karstic
528 structures over the field scale. This hypothesis is supported by the maps of the amplitude in
529 the models. Amplitude responses to a 2 min pumping signal in P15 quickly decease around
530 the borehole but remain visible in the coarse network over almost the entire field, while the
531 ones to a 5 min pumping signal stay high in the dense karstic network around P15, and
532 decrease beyond (Figure 8).

533 Concerning the property values, it appears that the reproduction of the responses required
534 more modifications on the transmissivity values than on the storativity, especially for the
535 conduits. Some similarities appear between the results to both periods, for example the
536 existence of conduits near P9 with lower transmissivities, which can then be assimilated more
537 likely to large fissures rather than conduits. Also in both results the conduits around P15 have
538 been associated to very high transmissivities (> 1 m^2/s), which tends to indicate the existence
539 of a very productive conduit at this position. This information could already been deduced by
540 the fact that the responses induced by a pumping in P15 in the model were slightly
541 overestimated (Figure 7).

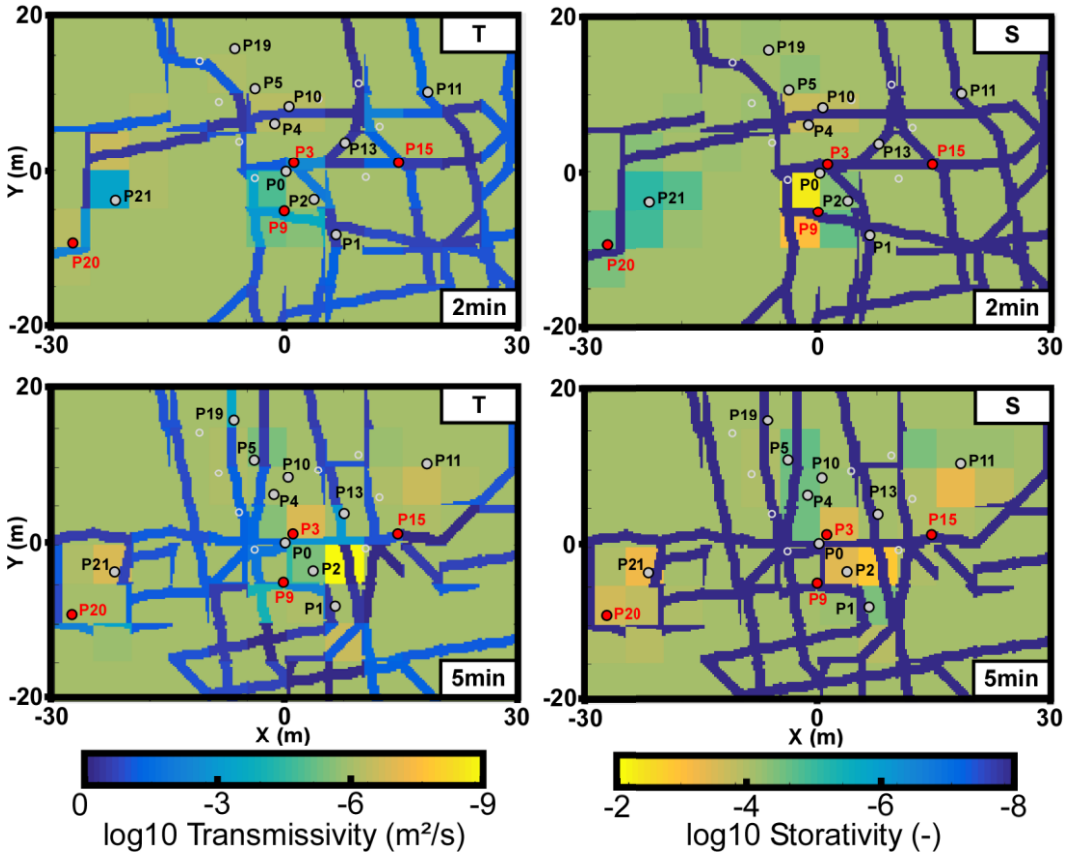

542

543 Figure 9: Maps of the distributions of transmissivity (T) and storativity (S) found by
544 separate inversions of the responses to periods of 2 min and 5 min.

545

546 The fact that the two periods of signal lead to different solutions to the inverse problem, even
547 by starting from a same initial model, tends to indicate that different periods of pumping
548 signal induce different flow fields in the tested karst aquifer. In order to better understand the
549 benefits of each period in a harmonic pumping characterization, one would need to study the
550 results of the joint inversions, led with the responses to both periods simultaneously.

551 ## 4.3. Effect of the period of pumping signal on the inversion results

552 It appears, in fact (see Table 3), that the separate models can badly simulate the responses
553 associated to the signal period not used in each inversion (i.e. 5 min responses simulated
554 through the model generated with 2 min responses, and conversely), suggesting that each set
555 of response contains different and complementary information for the characterization of the

556 field. Therefore, new inversions were started from the results presented in Figure 9 as initial
557 models, by joining the missing responses to the 'observed responses' dataset in the inverse
558 process (see the joint inversion results in Figure 6). For a better understanding, we will
559 mention as '2 min' and '5min' separate results the model results in Figure 9 produced from
560 the inversion of the responses to the 2 min and 5 min periods separately. The models
561 produced by inversions of the joint datasets started with the '2 min' model and with the '5
562 min' model will be respectively mentioned as the '2 min (+5 min)' and '5 min (+2 min)' joint
563 results. The results of the joint inversions are presented in Figure 10.

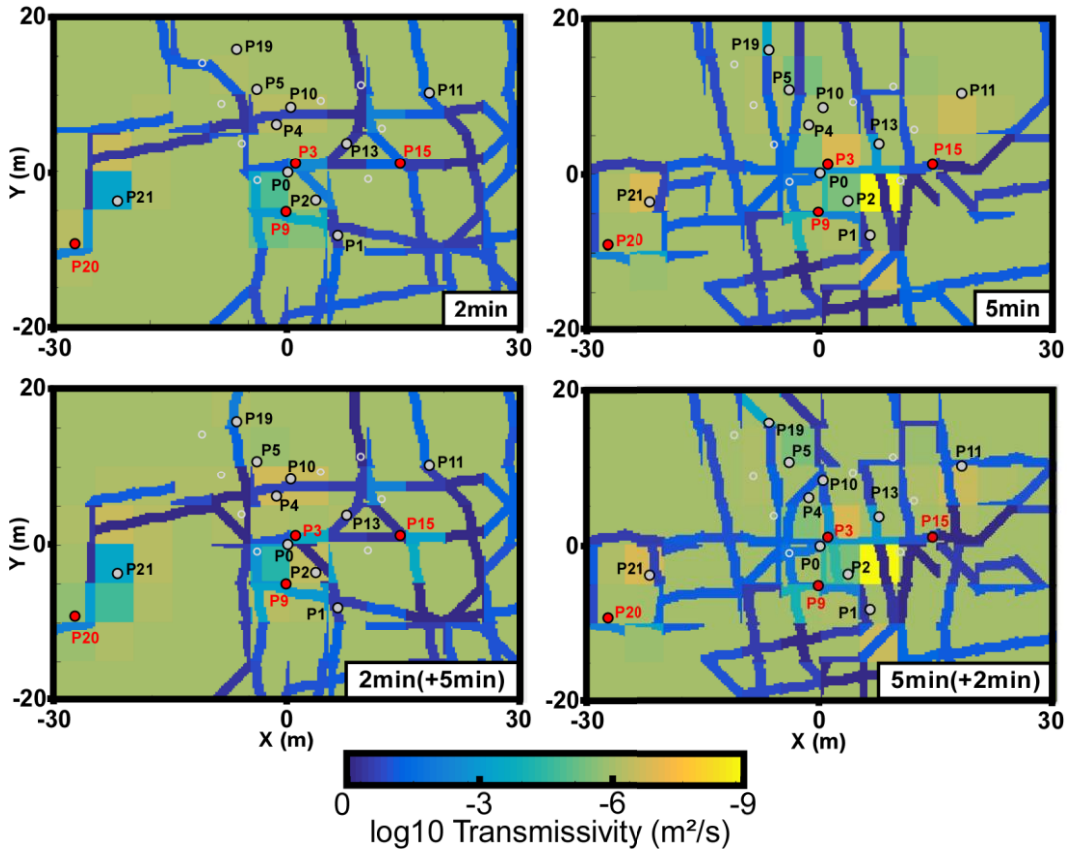

564

565 Figure 10: Maps of the distributions of transmissivity found by inversions of the responses to
566 the 2 min and 5 min periods, and joint inversions started with the 2 min result (2 min (+5
567 min)), and with the 5 min result (5 min (+2 min)).

568

569 The '2 min (+5 min)' result, solution to the inversion started from the '2 min' result, is very
570 close to its initial model. The '5 min (+2 min)' result, solution to the inversion started from

571 the ‘5 min’ result, shows some modifications on the periphery of its network (P4, P5, P10,
572 P11). Both joint solutions, however, do not permit a reproduction of the measured signals as
573 good as the one generated by the ‘2 min’ and ‘5 min’ separate results (see Table 3).

574 Table 3: RMSEs on the amplitude (Amp.) and phase offset (P.-O.) values for the different
575 inversion results. RMSEs values in brackets represent responses that were simulated through
576 models generated for another period of signal (i.e. 5 min responses simulated with a model
577 generated specifically for the 2 min responses and vice versa).

Results RMSEs		**‘2 min’**	**‘5 min’**	**‘2 min (+5 min)’**	**‘5 min (+2 min)’**
Amp.	**2 min**	1.1 cm	(11 cm)	5.4 cm	5.1 cm
	5 min	(9 cm)	0.5 cm	5 cm	5.3 cm
P.-O.	**2 min**	56 °	(112 °)	60 °	60 °
	5 min	(85 °)	66 °	67 °	66 °

578

579 Although the phase offsets RMSEs are almost the same for the joint results and the separate
580 results, the amplitudes RMSEs are multiplied by 5 to 10 with the joint results. This shows
581 that, even if the amplitude responses can be well reproduced by separate models for each
582 period, they cannot be reproduced very well with a unique model. This tends to validate the
583 hypothesis that different periods of pumping signal induce different flow fields in the aquifer,
584 which need to be characterized separately. In fact, the CADI method is limited in its ability to
585 represent a variation of aperture in the generated network, which can partly explain why the
586 joint inversions are less good than the separate ones if the flows mobilized with each period
587 occur in structures of different apertures.

588 However, even if the preferential flows change among the field for different pumping periods,
589 the relative distance of each borehole toward the karstic network does not depend on the
590 hydrodynamic but on the morphology of the karst structures, and thus their connectivity
591 behavior should logically remain the same as the karst structure does not vary with the period
592 of pumping. This is also what the reproduction of the phase offset values in the joint results
593 would tend to indicate. In fact, according to Figure 8, if the area of propagation of the

amplitude response is dependent to the density of the conduit network at that scale, it is not true for its phase offset which remains null in the conduits regardless of the network geometry.

In Table 4 we present the interpretation of the position of each borehole relatively to the conduits network, with the data processing estimations, the separate modeling results and the joint modeling results. First, it is interesting to point out that the estimations made manually in Figure 4 for the P15 pumping match for 62 % in term of position (in the conduit, close to a conduit, in the matrix) the separate modeling results '2 min' and '5 min'. Taking account that the estimation were made with only 13 responses over the 52 available, it shows that the manual interpretation method described in section 2.4 and in Fischer et al. (2018b) can already provide rather interesting and fast estimations.

Table 4: Positioning or connectivity response of each borehole interpreted from the qualitative estimations (Figure 4), the separate inversion results (Figure 9), and the joint inversion results (Figure 10).

Notation:

× : in a conduit = conduit connectivity response

⊗ : close to a conduit (< 0.5 m) = conduit connectivity response

○ : close to a conduit (< 2 m) = dual connectivity response

– : in the matrix = matrix connectivity response

	PERIOD = 2 MIN			**PERIOD = 5 MIN**			
	Est.	**Sep.**	**Joint**	**Joint**	**Sep.**	**Est.**	
P0	○	⊗	⊗	×	×	×	**P0**
P1	×	×	×	⊗	⊗	○	**P1**
P2	○	○	○	○	○	×	**P2**
P3		×	×	×	⊗		**P3**
P4	–	○	○	○	–	–	**P4**
P5	○	–	–	–	○	○	**P5**
P9	○	⊗	⊗	×	×	○	**P9**
P10	–	⊗	⊗	×	–	–	**P10**
P11	×	×	×	×	–	×	**P11**
P13	×	×	×	×	×	○	**P13**
P15	×	×	×	×	×	×	**P15**
P19	○	–	×	×	×	×	**P19**
P20	○	○	○	○	○	×	**P20**

P21 ○ _ _ ⊗ ⊗ ○ **P21**

According to Figure 8, the amplitude and phase offset responses of an observable point very close to a conduit (< 0.5 m) are almost undistinguishable to the ones directly in a conduit. Therefore we consider these points to also have a conduit connectivity response in Table 4. Figure 11 maps represent the interpreted connectivity of each borehole obtained from the joint inversion results. This figure also shows that these results reproduce the schema of connectivity of the preferential flow path established in Jazayeri Noushabadi (2009) and Dausse (2015) between P2, P11, P15, and P20 (see Figure 1).

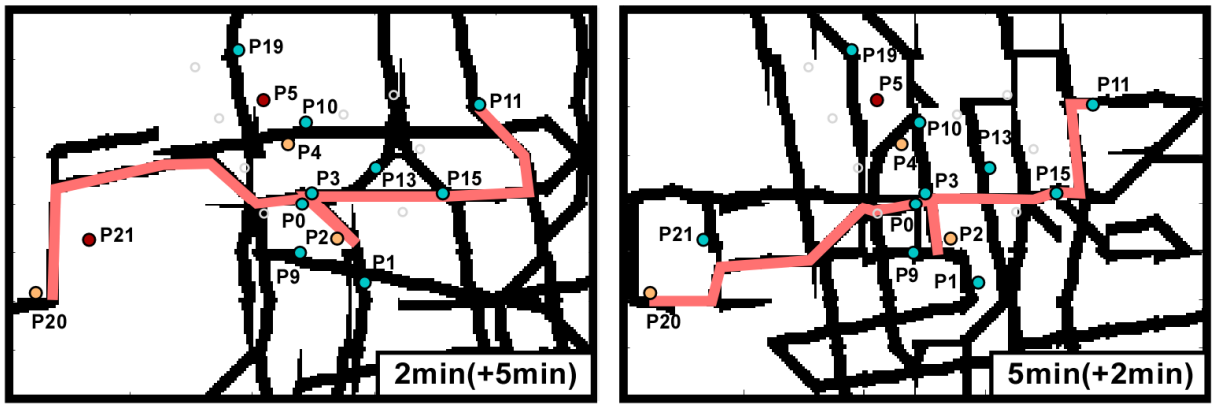

Figure 11: Maps of the connectivity responses associated to each borehole from the networks (shown in background in black) inverted with the joints inversions. Boreholes in blue are associated to a conduit connectivity, in orange to a dual connectivity, and in red to a matrix connectivity. The red lines show flow paths in the models which show a same connectivity as the field preferential flow path highlighted in Jazayeri Noushabadi (2009) and Dausse (2015).

Taking into account the connectivity response, 57 % of the boreholes show a similar behavior between the '2 min' and the '5 min' separate results. This degree of similarity increases to 93 % when comparing the boreholes connectivity responses from the two joint results. The only behavior difference between the two results comes from P21, which appears as connected through the matrix in the '2 min (+5 min)' result and as connected through conduits in the '5 min (+2 min)' result. However the property distribution of the '2 min (+5 min)' result in

Figure 10 shows that its matrix transmissivity near the P21 point has a value close to a conduit transmissivity. This permits to induce a conduit connectivity behavior for P21, even if the conduit is distant from the borehole. Therefore, we can consider that P21 should have a 'conduit connection behavior'. The fact that the degree of similarity of the boreholes behavior has increased to almost 100 % for two joint result clearly shows that the reproduction of the whole responses dataset requires to delineate a unique connectivity relation between each borehole, even if it is not sufficient to reproduce the amplitudes of the measured responses.

The remaining question is: which period of signal contains this information, as the separate results show only a 57 % similarity? The conduits network almost didn't change during the joint inversion started from the '2 min' result, and in fact, the separate '2 min' result and the joint '2 min (+5 min)' result show a 93 % similarity in their borehole behaviors, while the '5 min' result has a degree of similarity of 71 % with '5 min (+2 min)'. Then, most of the borehole behaviors found in the joint results were already present in the result of the 2 min signal period, which indicates that the 2 min responses contain the most information about the connectivity of each borehole.

If the two sets of amplitude responses are not well reproduced by the joint inversion while they both delineate a similar type of response for each borehole, it shows that the characterized property distribution (*in extenso* the induced flow paths network) is different for each period. In fact, the responses to a 5 min period require a dense flow network to be reproduced, while the responses to a 2 min period require a much more dispersed network. The structural posterior uncertainty maps in Figure 12 indicate that the network of the '2 min' result is very uncertain compared to the network of the '5 min' result. This indicates that the responses to a 5 min period contain more information on the localization of the flow paths around the measurement points than the responses to a 2 min period. These last ones seem to provide less precise information on the localization of the flows between the boreholes among

659 the field. When inverting jointly the responses from the two period, the networks in the joint
660 results show overall lower uncertainties. Globally, the study of the structural uncertainties
661 tends to indicate that, while, as seen before, responses to a the lower period contain more
662 information on the type of connectivity of each borehole, the responses to the higher period
663 contain more information on the position of the preferential flow paths around the boreholes.
664 However, the fact that these both sets of responses cannot be well reproduced simultaneously
665 also indicates that the flows highlighted in the '5 min' result do not exist with a period of 2
666 min. Therefore, while the lower period essentially mobilizes water from the most conductive
667 karstic structures among the field, the dense flow field highlighted by the higher period can be
668 assimilated to a mobilization of water also in less conductive karstic structures.

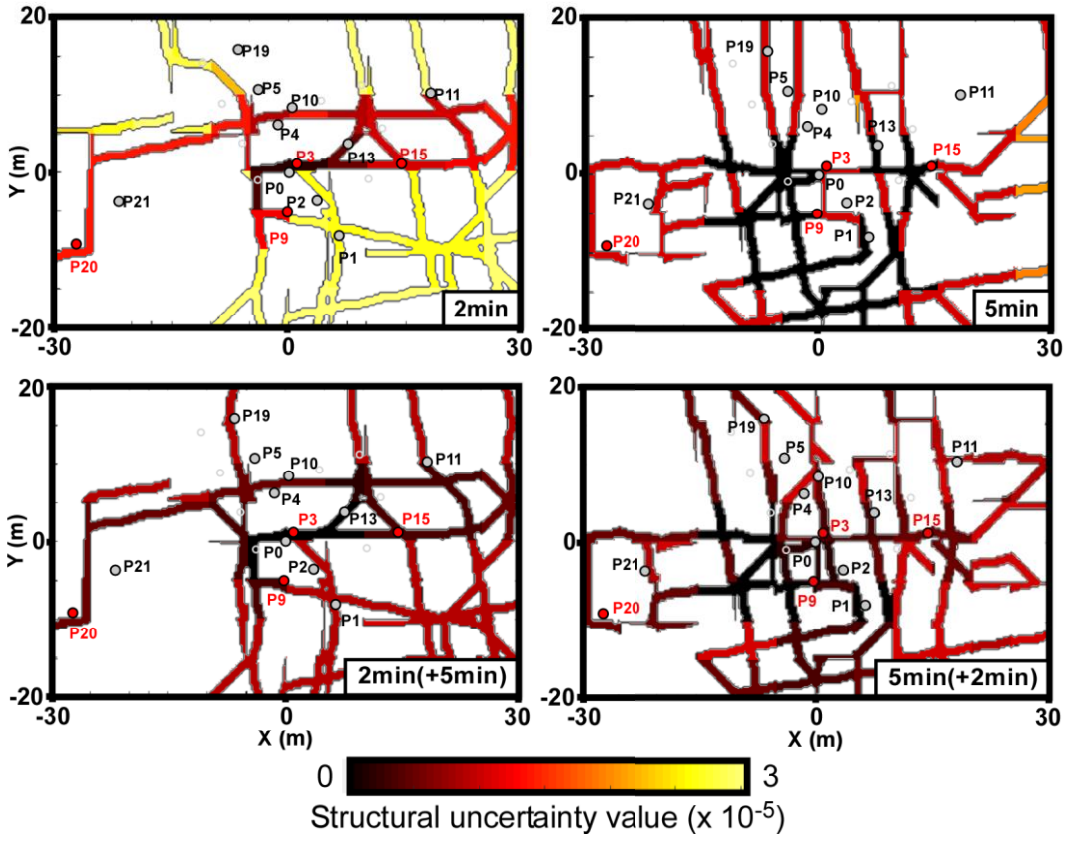

669

670 Figure 12: Structural uncertainty values from the results found for separate inversions of the 2
671 min and 5 min responses, and joint inversions started with the 2 min result (2 min (+5 min)),
672 and with the 5 min result (5 min (+2 min)).

673

674 The maps of the posterior uncertainties on the transmissivity values in Figure 13 tend to show
675 that the responses to a 2 min period give more information on the transmissivity of conduits
676 locally around the pumping points (average ± 0.1 on the transmissivity exponent) than the
677 responses to a 5 min period (± 0.2 on the transmissivity exponent). The uncertainties on the
678 storativity values remain high in the whole conduit network and for both periods (± 0.2 on the
679 storativity exponent). Further from the pumping boreholes, both property values in the
680 conduits network (transmissivity and storativity) globally remain uncertain (± 0.3 on the
681 exponent), even in the joint results. The transmissivity and storativity values in the matrix are
682 more constrained around the measurement points in the matrix. These information indicate
683 that, for both periods, the characterization of the property values with oscillatory responses
684 remains local, around the boreholes. Oscillatory responses provide more information on the
685 global connectivity and the localization of preferential flows rather than on the property
686 values of the matrix and the conduits and fissures in the aquifer.

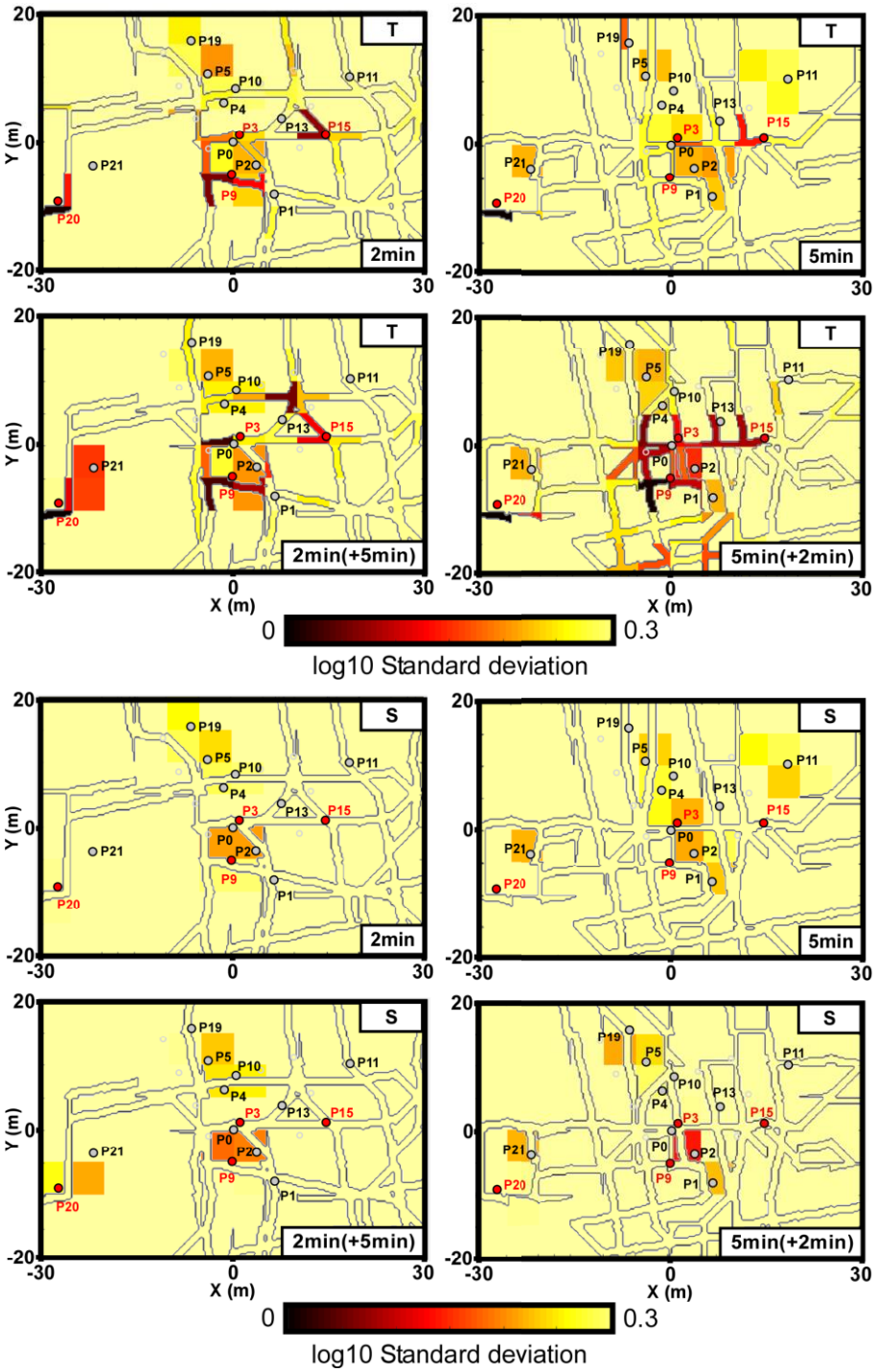

687

688 Figure 13: Transmissivity (T) and storativity (S) standard deviation values of the results
689 found for separate inversions of the 2 min and 5 min responses, and joint inversions started
690 with the 2 min result (2 min (+5 min)), and with the 5 min result (5 min (+2 min)).

691

692 Overall, regarding our results, it appears that the flow paths generated by periods of 2 min and

693 a 5 min in the pumping signals in this karstic field are very different. It appears in fact that, at

694 our field scale, higher frequency signals (here a period of 2 min) activate principally the most
695 conductive flow paths over the field, mostly located in the conduits network. These
696 frequencies permit to better characterize the distance between each borehole and the most
697 conductive karstic structures. Therefore, they allow a better interpretation of a degree of
698 connectivity between boreholes, through the network of karstic conduits. Lower frequency
699 signals (here a period of 5 min) activate, at our field scale, both conductive and also less
700 conductive structures. Therefore, these frequencies permit to better characterize the existence
701 and the localization of networks of fractures and fissures around the boreholes.

702 5. Discussion

703 In Fischer et al. (2018b), the authors have described a qualitative method for interpreting
704 inter-well connectivity from the responses to harmonic pumping tests in karstic aquifers, by
705 categorizing the extracted oscillatory responses in three types (conduit, dual, matrix
706 connectivity). In this work the method is further developed through the integration of a
707 quantitative interpretation with an inverse algorithm, the CADI method, that can handle a
708 large number of measured data simultaneously and generate complex distributions of
709 properties. The integrated approach permits to produce spatial distributions of amplitude and
710 phase offset responses consistent with those studied by Fischer et al. (2018b).

711 The comparison of inverted conduit networks from periods of 2 min and 5 min indicates
712 different pumping frequency generate different flow fields. A higher frequency will permit to
713 better characterize the flows in highly conductive structures, and the conduit connectivity at a
714 field scale. This finding is consistent with the work of Rabinovich et al. (2015) where the
715 authors show that the flow paths tend to follow the most conductive media especially at lower
716 period. On the contrary, a lower frequency will permit to better characterize the flows in less
717 conductive structures, and thus the localization of networks of smaller conduits, fractures and

718 fissures. Each frequency of signal permits to generate responses holding different and
719 complementary information on karst structures. There is therefore, according to our results, no
720 'best' choice of period for the characterization of a karstic field. This choice should be made
721 accordingly to what structures one would most likely characterize. The important impact of
722 the period of the pumping signal on the ratio of conduit/matrix flows has already been
723 highlighted with a simplified study case in Fischer et al. (2018b), but our new work also
724 shows a more complex role of the different structures (conduit, fracture, fissure, matrix) on
725 the generation of different flow fields with the different frequencies of pumping signal.

726 To summarize, if at a regional scale one would imagine that the difference between a lower
727 and a higher frequency pumping would principally concern the zone of influence in the
728 aquifer (with a larger zone for a lower frequency), this difference implies more specific
729 behaviors at a smaller site scale. In fact, at this scale, higher frequencies mobilize water
730 essentially in the most conductive structures, while lower frequencies permit to reach also a
731 mobilization of water in the less conductive structures and media. On another hand oscillatory
732 responses do not provide precise information on the conductivity and specific storage values
733 in the conduits and the matrix very far from the pumping point. However the same
734 observation was made on the same field for the inversion of steady-state responses to eight
735 pumping tests at constant rates in Fischer et al. (2017c). This previous article also showed that
736 steady state data to constant rate pumping (comparable to an infinitely high oscillatory period)
737 were more sensitive to fracture flows and required a dense inverted network to be reproduced,
738 which is in agreement with our observation for a higher period of signal in this work.
739 Furthermore, the uncertainty analysis from this previous article indicated that the constant rate
740 data, as the data for a period of 5 min in the pumping signal in this work, permitted to better
741 characterize the flow structures in areas where we had measurement points. The inverted
742 networks in the results from our new work and the ones in Fischer et al. (2017c) both

743 reproduce the established connectivity of the Terrieu field (Jazayeri Noushabadi 2009 ;
744 Dausse 2015), but in the case of the constant rate data, the inversions were led with responses
745 to an investigation of eight pumping points instead of four with the harmonic investigation.

746 The results of our new work, associated to the previous ones in Fischer et al. (2017c), tend to
747 indicate that the steady state responses to a constant pumping rate would blur the connectivity
748 associated to the most conductive conduits among the field, while better characterizing the
749 karstic structures of different scales in the areas around the pumping wells. Therefore it would
750 require several well distributed pumping points in order to characterize the whole karstic
751 network. Responses to an oscillatory pumping rate, on contrary, allow an already good
752 characterization of the karstic connectivity from a unique pumping in a borehole in the karstic
753 network (as P15 in this work).

754 6. Conclusion

755 In this work we have extended the qualitative method presented in Fischer et al. (2018b), for
756 interpreting a karstic network connectivity from the hydraulic responses to harmonic pumping
757 tests, to a quantitative analysis by combining these responses with an inversion algorithm. The
758 integrated approach is able to deal with a large set of data simultaneously and to construct
759 structurally contrasted distributions of hydraulic properties conditioned to the measured
760 tomographic harmonic pumping responses.

761 Our results show that tomographic harmonic pumping tests performed with different signal
762 frequencies led to a characterization of different structures of the karstic network. Higher
763 frequency signals tend to assist in interpreting a degree of connectivity between each borehole
764 of the field and the most conductive structures, while lower frequency signals are more useful
765 in the localization of less conductive features, such as small fractures and fissures.

766 The CADI method, as imaging tool, shows limitations in its ability to represent complex
767 structures of different aperture simultaneously, as already noticed in Fischer et al. (2017c),
768 which can partly explain the less good results of the joint inversions compared to the separate
769 inversions in this work. However we believe that the combination of the CADI method with
770 tomographic harmonic pumping tests appears as a promising methodology for a quantitative
771 characterization of the hydraulic properties and the hydraulic connectivity in karstic aquifers.

772 ## Acknowledgments

773 We would like to thank Todd C. Rasmussen and two anonymous reviewers for their relevant
774 comments and propositions which permitted to significantly improve the quality of this
775 article. We thank the Normandy region for providing financial support for the PhD of Pierre
776 Fischer. We also thank Michel Simon for his precious contribution during the field
777 investigation. The hydraulic data collection and hydrogeological characterization of the
778 Terrieu experimental site are part of work of the French research network SNO Karst.

Appendix

Appendix 1: Interpreted amplitude and phase offset responses for both signal periods (2 min, 5 min) of each pumping point (P3, P9, P15, P20) and distances between the measurement points and the pumping points. A dash represents a negligible oscillatory response (amplitude lower than 1 mm). Dashes represent a negligible oscillatory response, considered as null for the inversion.

	P3					P9				
	Distance (m)	Amplitude (cm)		Phase offset (°)		Distance (m)	Amplitude (cm)		Phase offset (°)	
		2 min	5 min	2 min	5 min		2 min	5 min	2 min	5 min
P0	1.4	2.30	2.40	27	11	5.3	0.20	0.11	0	24
P1	10.6	0.17	0.17	-53	145	7.2	0.33	0.14	0	-110
P2	5.4	--	--	--	--	4.2	0.26	0.66	109	88
P4	5.7	--	--	--	--	11.4	--	--	--	--
P5	11	0.18	0.20	151	-126	16.4	0.22	0.23	143	82
P9	6.3	0.20	0.47	104	71	--	18	31	39	54
P10	7.5	--	--	--	--	13.7	--	--	--	--
P11	19.4	0.19	0.18	-20	41	24	0.17	0.12	0	-97
P13	6.9	0.33	0.22	40	85	11.7	0.18	0.14	143	0
P15	13.3	--	--	--	--	15.9	0.26	0.16	112	166
P19	16.7	0.13	0.11	-172	-25	22	0.27	0.11	110	-134
P20	30.1	--	--	--	--	27.3	--	--	--	--
P21	23.3	--	--	--	--	21.6	--	--	--	--

	P15					P20				
	Distance (m)	Amplitude (cm)		Phase offset (°)		Distance (m)	Amplitude (cm)		Phase offset (°)	
		2 min	5 min	2 min	5 min		2 min	5 min	2 min	5 min
P0	14.4	0.27	0.42	41	52	28.9	0.38	0.24	-7	68
P1	12.4	0.36	0.18	-39	154	33.6	0.37	0.15	6	-76
P2	11.7	0.29	0.39	49	46	31.5	0.24	0.26	3	64
P4	16.6	--	--	--	--	30.1	--	--	--	--
P5	20.7	0.18	0.19	166	79	30.9	0.25	0.14	17	135
P9	15.9	0.22	0.28	-22	82	27.3	0.26	0.20	14	114
P10	15.8	--	--	--	--	32.9	--	--	--	--
P11	9.9	0.37	0.49	13	34	49.5	0.33	0.26	11	68
P13	7.3	0.52	0.23	-76	-168	37.1	0.23	0.15	5	-9
P15	--	1.40	1.30	-22	8	43	0.46	0.35	3	56
P19	25.6	0.14	0.26	14	66	32.7	0.14	0.15	-78	84
P20	43	0.27	0.34	64	53	--	93	153	41	3
P21	36.5	0.33	0.22	-180	89	7.9	0.24	0.21	-8	98

References

Abusaada, M. and M. Sauter. 2013. Studying the flow dynamics of a karst aquifer system with an equivalent porous medium model. *Groundwater* 51 (No. 4): 641-650

Ackerer, P., and F. Delay. 2010. Inversion of a set of well-test interferences in a fractured limestone aquifer by using an automatic downscaling parameterization technique. *Journal of Hydrology* 389: 42-56.

Bakhos, T., M. Cardiff, W. Barrash, and P.K. Kitanidis. 2014. Data processing for oscillatory pumping tests. *Journal of Hydrology* 511: 310-319.

Berg, S.J., and W.A. Illman. 2013. Field study of subsurface heterogeneity with steady-state hydraulic tomography. *Groundwater* 51 (No. 1): 29-40.

Bohling, G.C., X. Zhan, J.J. Butler, and L. Zheng. 2002. Steady shape analysis of tomographic pumping tests for characterization of aquifer hetereogeneities. *Water Resources Research* 38: 1324.

Bonneau, F., V. Henrion, G. Caumon, P. Renard, and J. Sausse. 2013. A methodology for pseudo-genetic stochastic modeling of discrete fracture networks. *Computer & Geosciences* 56: 12-22.

807 Borghi, A., P. Renard, and F. Cornaton. 2016. Can one identify karst conduit networks
808 geometry and properties from hydraulic and tracer test data? *Advances in Water Resources*
809 90: 99-115.

810

811 Butler, J.J. 2005. Hydrogeological methods for estimation of spatial variations in hydraulic
812 conductivity. In: Rubin, Y., S.S. Hubbard. Hydrogeophysics. Water Science and Technology
813 Library (vol. 50). Springer, Dordrecht.

814

815 Caers, J. and T. Hoffman. 2006. The probability perturbation method: A new look at Bayesian
816 inverse modeling. *Mathematical Geology* 38 (No. 1): 81-100.

817

818 Cardiff, M., W. Barrash, P.K. Kitanidis, B. Malama, A. Revil, S. Straface, and E. Rizzo.
819 2009a. A potential-based inversion of unconfined steady-state hydraulic tomography.
820 *Groundwater* 47 (No. 2): 259-270.

821

822 Cardiff, M., and P.K. Kitanidis. 2009b. Bayesian inversion for facies detection: An extensible
823 level set framework. *Water Resources Research* 45: W10416, doi: 10.1029/2008WR007675.

824

825 Cardiff, M., W. Barrash, and P.K. Kitanidis. 2013a. Hydraulic conductivity imaging from 3-D
826 transient hydraulic tomography at several pumping/observation densities. *Water Resources*
827 *Research* 49: 7311-7326.

828

829 Cardiff, M., T. Bakhos, P.K. Kitanidis, and W. Barrash. 2013b. Aquifer heterogeneity
830 characterization with oscillatory pumping: Sensitivity analysis and imaging potential. *Water*
831 *Resources Research* 49: 5395-5410.

832

833 Cardiff, M. and W. Barrash. 2015. Analytical and semi-analytical tools for the design of
834 oscillatory pumping tests. *Groundwater* 53 (No. 6): 896-907.

835

836 Carrera, J., and S.P. Neuman. 1986. Estimation of aquifer parameters under transient and
837 steady state conditions: 1. Maximum likelihood method incorporating prior information.
838 *Water Resources Research* 22 (No. 2) : 199-210.

839

840 Castagna, M., M.W. Becker, A. Bellin. 2011. Joint estimation of transmissivity and storativity
841 in a bedrock fracture. *Water Resources Research* 47: W09504 doi: 10.1029/2010WR009262.

842

843 Collon, P., D. Bernasconi, C. Vuilleumier, and P. Renard. 2017. Statistical metrics for the
844 characterization of karst network geometry and topology. *Geomorphology* 283: 122-142.

845

846 Dausse, A. 2015. Facteurs d'échelle dans la hiérarchisation des écoulements au sein d'un
847 aquifère karstique : Analyse multi-échelles des propriétés hydrodynamiques et de transport de
848 l'aquifère de Lez. PhD Thesis, Université de Montpellier. French.

849

De Rooij, R., P. Perrochet, W. Graham. 2013. From rainfall to spring discharge: coupling conduit flow, subsurface matrix flow and surface flow in karst systems using a discrete-continuum model. *Advances in Water Resources* 61: 29-41.

Fischer, P., A. Jardani, A. Soueid Ahmed, M. Abbas, X. Wang, H. Jourde, N. Lecoq. 2017a. Application of large-scale inversion algorithms to hydraulic tomography in an alluvial aquifer. *Groundwater* 55: 208-218.

Fischer, P., A. Jardani, N. Lecoq. 2017b. A cellular automata-based deterministic inversion algorithm for the characterization of linear structural heterogeneities. *Water Resources Research* 53: 2016-2034.

Fischer, P., A. Jardani, X. Wang, H. Jourde, N. Lecoq. 2017c. Identifying Flow Networks in a Karstified Aquifer by Application of the Cellular Automata-based Deterministic Inversion Method (Lez Aquifer, France). *Water Resources Research* 53: 10508-10522.

Fischer, P., A. Jardani, N. Lecoq. 2018a. Hydraulic Tomography of Discrete Networks of Conduits and Fractures in a Karstic Aquifer by Using a Deterministic Inversion Algorithm. *Advances in Water Resources* 112: 83-94.

Fischer, P., A. Jardani, M. Cardiff, H. Jourde, N. Lecoq. 2018b. Hydraulic Analysis of Harmonic Pumping Tests in Frequency and Time Domains for Identifying the Conduits

872 Networks in a Karstic Aquifer. *Journal of Hydrology* In Press, doi:
873 10.1016/j.jhydrol.2018.03.010.

874

875 Ghasemizadeh, R., F. Hellweger, C. Butscher, I. Padilla, D. Vesper, M. Field, and A.
876 Alshawabkeh. 2012. Review: Groundwater flow and transport modeling of karst aquifers,
877 with particular reference to the North Coast Limestone aquifer system of Puerto Rico.
878 *Hydrogeology Journal* 20: 1441-1461.

879

880 Grimstadt, A.-A., T. Mannseth, G. Naevdal, H. Urkedal. 2003. Adaptive multiscale
881 permeability estimation. *Computers & Geosciences* 7: 1-25.

882

883 Guiltinan, E., and M.W. Becker. 2015. Measuring well hydraulic connectivity in fractured
884 bedrock using periodic slug tests. *Journal of Hydrology* 521: 100-107.

885

886 Hao, Y., T.J. Yeh, J. Xiang, W.A. Illman, K. Ando, K. Hsu, and C. Lee. 2008. Hydraulic
887 tomography for detecting fracture zone connectivity. *Ground Water* 46: 183–192.

888

889 Hartmann, A., N. Goldscheider, T. Wagener, J. Lange, and M. Weiler. 2014. Karst water
890 resources in a changing world: Review of hydrological modeling approaches. *Reviews of*
891 *Geophysics* 52: 218-242.

892

893 Hoeksema, R.J., and P.K. Kitanidis. 1984. An application of the geostatistical approach of the
894 inverse problem in two-dimensional groundwater modeling. *Water Resources Research* 20:
895 1003-1020.

896

897 Illman, W.A., X. Liu, S. Takeuchi, T.J. Yeh, K. Ando, and H. Saegusa. 2009. Hydraulic
898 tomography in fractured granite: Mizunami underground research site, Japan. *Water*
899 *Resources Research* 45 doi: 10.1029/2007WR006715.

900

901 Illman, W.A. 2014. Hydraulic tomography offers improved imaging of heterogeneity in
902 fractured rocks. *Groundwater* 52: 659-684.

903

904 Jaquet, O., P. Siegel, G. Klubertanz, and H. Benabderrhamane. 2004. Stochastic discrete
905 model of karstic networks. *Advances in Water Resources* 27: 751-760.

906

907 Jazayeri Noushabadi, M.R. 2009. Characterization of relationship between fracture network
908 and flow-path network in fractured and karstic reservoirs: Numerical modeling and field
909 investigation (Lez aquifer, Southern France). PhD Thesis, Université de Montpellier. English.

910

911 Jazayeri Noushabadi, M.R., H. Jourde, G. Massonnat. 2011. Influence of the observation scale
912 on permeability estimation at local and regional scales through well tests in a fractured and
913 karstic aquifer (Lez aquifer, Southern France). *Journal of Hydrology* 403: 321-336.

914

915 Jourde, H., F. Cornaton, S. Pistre, P. Bidaux. 2002. Flow behavior in a dual fracture network.
916 *Journal of hydrology* 266: 99-119.

917

918 Jourde, H., et al. 2011. The MEDYCYSS observatory, a multi scale observatory of flood
919 dynamics and hydrodynamics in karst (Mediterranean border Southern France). In:
920 Lambrakis, N., G. Stournaras, K. Katsanou. Advances in the research of aquatic environment.
921 *Environmental Earth Sciences*. Springer, Berlin, Heidelberg.

922

923 Kitanidis, P.K. 1995. Quasi-linear geostatistical theory for inversing. *Water Resources*
924 *Research* 31 (No. 10): 2411-2419.

925

926 Kovacs, A. 2003. Estimation of conduits network geometry of a karst aquifer by the means of
927 groundwater flow modeling (Bure, Switzerland). *Boletin Geologico y Minero* 114 (No. 2):
928 183-192.

929

930 Larocque, M., O. Banton, P. Ackerer, and M. Razack. 1999. Determining karst
931 transmissivities with inverse modeling and an equivalent porous media. *Ground Water* 37
932 (No. 6): 897-903.

933

934 Lavenue, M., and G. de Marsily. 2001. Three-dimensional interference test interpretation in a
935 fractured aquifer using the pilot point inverse method. *Water Resources Research* 37 (No. 11):
936 2659-2675.

Le Coz, M., J. Bodin, and P. Renard. 2017. On the use of multiple-point statistics to improve groundwater flow modeling in karst aquifers: a case study from the hydrogeological experimental site of Poitiers, France. *Journal of Hydrology* 545: 109-119.

Lee, J., and P.K. Kitanidis. 2013. Bayesian inversion with total variation prior for discrete geologic structure identification. *Water Resources Research* 49: 7658–7669.

Li, Z.Y., J.H. Zhao, X.H. Qiao, and Y.X. Zhang. 2014. An automated approach for conditioning discrete fracture network modelling to in situ measurements. *Australian Journal of Earth Sciences* 61: 755-763.

Liedl, R., M. Sauter, D. Huckinghaus, T. Clemens, G. Teutsch. 2003. Simulation of the development of karst aquifers using a coupled continuum pipe flow model. *Water Resources Research* 39, 1057.

Lochbühler, T., J.A. Vrugt, M. Sadegh, and N. Linde. 2015. Summary statistics from training images as prior information in probabilistic inversion. *Geophysical Journal International* 201: 157–171.

Lu, Z., and B.A. Robinson. 2006. Parameter identification using the level set method. *Geophysical Research Letters* 33: L06404, doi: 10.1029/2005GL025541.

Maineult, A., E. Strobach, and J. Renner. 2008. Self-potential signals induced by periodic pumping tests. *Journal of Geophysical Research* 113: B01203 doi: 10.1029/2007JB005193.

Ni, C., and T.J. Yeh. 2008. Stochastic inversion of pneumatic cross-hole tests and barometric pressure fluctuations in heterogeneous unsaturated formations. *Advances in Water Resources* 31: 1708-1718.

Pardo-Iguzquiza, E., P.A. Dowd, C. Xu, and J.J. Duran-Valsero. 2012. Stochastic simulation of karst conduit networks. *Advances in Water Resources* 35: 141-150

Rabinovich, A., W. Barrash, M. Cardiff, D.L. Hochstetler, T. Bakhos, G. Dagan, P.K. Kitanidis. 2015. Frequency dependent hydraulic properties estimated from oscillatory pumping tests in an unconfined aquifer. *Journal of Hydrology* 531: 2-16.

Rasmussen, T.C., K.G. Haborak, and M.H. Young. 2003. Estimating aquifer hydraulic properties using sinusoidal pumping at the Savannah River site, South California, USA. *Hydrogeology Journal* 11: 466-482.

Renner, J., and M. Messar. 2006. Periodic pumping tests. *Geophysical Journal International* 167: 479-493.

981 Saller, A.P., M.J. Ronayne, and A.J. Long. 2013. Comparison of a karst groundwater model
982 with and without discrete conduit flow. *Hydrogeology Journal* 21: 1555-1566.

983

984 Sharmeen, R., W.A. Illman, S.J. Berg, T.J. Yeh, Y. Park, E.A. Sudicky, and K. Ando. 2012.
985 Transient hydraulic tomography in a fractured dolostone: laboratory rock block experiments.
986 *Water Resources Research* 48 doi: 10.1029/2012WR012216.

987

988 Soueid Ahmed, A., J. Zhou, A. Jardani, A. Revil, and J.P. Dupont. 2015. Image-guided
989 inversion in steady-state hydraulic tomography. *Advances in Water Resources* 82: 83–97.

990

991 Soueid Ahmed, A., A. Jardani, A. Revil, and J.P. Dupont. 2016. Joint inversion of hydraulic
992 head and self-potential data associated with harmonic pumping tests. *Water Resources*
993 *Research* 52 (No. 9): 6769-6791.

994

995 Sun, A. Y., J. Lu, and S. Hovorka. 2015. A harmonic pulse testing method for leakage
996 detection in deep subsurface storage formations. *Water Resources Research* 51: 4263–4281.

997

998 Tarantola, A. and B. Valette. 1982. Generalized nonlinear inverse problems solved using the
999 least squares criterion. *Reviews of Geophysics and Space Physics* 20, no.2: 219-232.

1000

1001 Teutsch, G. 1993. An extended double-porosity concept as a practical modeling approach for
1002 a karstified terrain. *Hydrogeological Processes in Karst Terranes* 207: 281-292.

Von Neumann, J. and A.W. Burks. 1966. Theory of self-reproducing automata. *University of Illinois Press* ISBN 0-598-37798-0.

Wang, X., A. Jardani, H. Jourde, L. Lonergan, J. Cosgrove, O. Gosselin, and G. Massonat. 2016. Characterisation of the transmissivity field of a fractured and karstic aquifer, Southern France. *Advances in Water Resources* 87: 106-121.

Wang, X., A. Jardani, and H. Jourde. 2017. A hybrid inverse method for hydraulic tomography in fractured and karstic media. *Journal of Hydrology* 551: 29-46.

White, W.B. 2002. Karst hydrology: recent developments and open questions. *Engineering Geology* 65: 85-105.

Yeh, T.J., and S. Liu. 2000. Hydraulic tomography: Development of a new aquifer test method. *Water Resources Research* 36: 2095-2105.

Yeh, T.J., and C. Lee. 2007. Time to change the way we collect and analyze data for aquifer characterization. *Groundwater* 45 (No. 2): 116-118.

1023 Zha, Y., T.J. Yeh, W.A. Illman, T. Tanaka, P. Bruines, H. Onoe, and H. Saegusa. 2015. What
1024 does hydraulic tomography tell us about fractured geological media? A field study and
1025 synthetic experiments. *Journal of Hydrology* 531 (No. 1): 17-30.

1026

1027 Zha, Y., T.J. Yeh, W.A. Illman, T. Tanaka, P. Bruines, H. Onoe, H. Saegusa, D. Mao, S.
1028 Takeuchi, and J.C. Wen. 2016. An application of hydraulic tomography to a large-scale
1029 fractured granite site, Mizunami, Japan. *Groundwater* 54: 793-804.

1030

1031 Zha, Y., T.J. Yeh, W.A. Illman, H. Onoe, C.M.W. Mok, J.C. Wen, S.Y. Huang, and W.
1032 Wang. 2017. Incorporating geologic information into hydraulic tomography: A general
1033 framework based on geostatistical approach. *Water Resources Research* 53:
1034 doi:10.1002/2016WR019185.

1035

1036 Zhou, Y., D. Lim, F. Cupola, and M. Cardiff. 2016. Aquifer imaging with pressure waves -
1037 Evaluation of low-impact characterization through sandbox experiments. *Water Resources*
1038 *Research* 52: 2141-2156.

1039

1040 Zhu, J., and T.J. Yeh. 2005. Characterization of aquifer heterogeneity using transient
1041 hydraulic tomography. *Water Resources Research* 41: W07028.